Coastal Engineering 152 (2019) 103526

Contents lists available at ScienceDirect

Coastal Engineering

journal homepage: www.elsevier.com/locate/coastaleng

A numerical study of sheet flow driven by velocity and acceleration skewed near-breaking waves on a sandbar using SedWaveFoam

Yeulwoo Kim[a,*], Ryan S. Mieras[b], Zhen Cheng[c], Dylan Anderson[d], Tian-Jian Hsu[a], Jack A. Puleo[a], Daniel Cox[d]

[a] Center for Applied Coastal Research, Department of Civil and Environmental Engineering, University of Delaware, Newark, DE, USA
[b] National Research Council, Postdoctoral Research Associate, Research Associateship Program, Marine Geosciences Division, U.S. Naval Research Laboratory, Stennis Space Center, MS, USA
[c] Convergent Science Inc., Madison, WI, USA
[d] Coastal and Ocean Engineering Program, School of Civil and Construction Engineering, Oregon State University, Corvallis, OR, USA

ARTICLE INFO

Keywords:
Sediment transport
Sheet flow
Momentary bed failure
Two-phase model
Progressive wave streaming
Wave-stirring effect

ABSTRACT

A new methodology capable of concurrently resolving free surface wave field, bottom boundary layer, and sediment transport processes throughout the entire water column was recently developed in the OpenFOAM framework, called SedWaveFoam. In this study, SedWaveFoam is validated with large wave flume data for sheet flow driven by near-breaking waves. Good agreements are obtained for free surface elevation, flow velocity, turbulence kinetic energy, sediment concentration, and sheet flow sediment fluxes. Model results are used to investigate the joint effects of velocity skewness, acceleration skewness, and progressive wave streaming on sheet flow sediment transport. SedWaveFoam results are contrasted with rigid-lid one-dimensional-vertical model results to isolate the effect of the free surface. Onshore directed near-bed flow velocity and sediment flux are enhanced due to the presence of the free surface via progressive wave streaming. However, the enhancement of net onshore sediment transport for the near-breaking condition with both high velocity and acceleration skewness is several factors greater than that found in the nonbreaking condition with only high velocity skewness. Model results suggest that the large horizontal pressure gradient, which has a Sleath parameter exceeding 0.2, may play a key role. Momentary bed failure is identified via near-bed instability of the sheet flow layer, associated with a large bed shear stress and horizontal pressure gradient. Instantaneous near-bed vortices due to the near-bed instability correspond to the increase of horizontal pore pressure gradient during the wave crest, consistent with measured data. Model inter-comparison suggests that a two-dimensional model is crucial to capture the effect of momentary bed failure that increases sediment suspension during wave crest passage and net onshore sediment transport.

1. Introduction

Sandbars are prominent nearshore bathymetric features where sediment transport and rapid morphological change can occur (Thornton et al., 1996; Gallagher et al., 1998; Aagaard et al., 2002; Ruggiero et al., 2005; Ruessink et al., 2009; Tissier et al., 2011; Grasso et al., 2012). Sandbars enhance depth-induced wave breaking and help determine the cross-shore evolution of wave shape and cross-shore and alongshore currents (Reniers et al., 2004), altering sediment transport patterns. Therefore, improved prediction of coastal morphological evolution is closely related to the understanding of onshore and offshore sediment fluxes driven by waves and currents that lead to cross-shore sandbar migration (Henderson et al., 2004; Hsu et al., 2006; Ruessink and Kuriyama, 2008; Fernández-Mora et al., 2015). However, a comprehensive understanding of sediment transport under surface waves does not yet exist due to many inter-connected mechanisms and uncertainties in their relative importance, such as: velocity skewness (Doering et al., 2000; Austin et al., 2009; Cheng et al., 2017); progressive wave streaming (Nielsen, 2006; Holmedal and Myrhaug, 2009; Kranenburg et al., 2012, 2013; Fuhrman et al., 2013; Kim et al., 2018); acceleration skewness (Drake and Calantoni, 2001; Foster et al., 2006); and wave-breaking turbulence (Voulgaris and Collins, 2000; Scott et al., 2009; Aagaard and Hughes, 2010; Yoon and Cox, 2010).

The significance of progressive wave streaming in driving onshore sediment transport for various grain sizes and wave conditions has been identified and quantified using 1DV boundary layer sediment transport

* Corresponding author.
E-mail address: ykim@udel.edu (Y. Kim).

https://doi.org/10.1016/j.coastaleng.2019.103526
Received 15 February 2019; Received in revised form 16 June 2019; Accepted 7 July 2019
Available online 10 July 2019
0378-3839/

models employing the relationship of $\partial/\partial x = -1\partial/C\partial t$ (e.g., Holmedal and Myrhaug, 2009; Fuhrman et al., 2013), in which C is the wave celerity. Recently, an open-source free surface resolving Eulerian two-phase sediment transport model, SedWaveFoam (Kim et al., 2018), was developed by combining two numerical models, SedFoam (Cheng et al., 2017) and InterFoam/waves2Foam (Berberović et al., 2009; Klostermann et al., 2012/Jacobsen et al., 2012), using the OpenFOAM CFD toolbox. By its design, SedWaveFoam concurrently resolves the free surface wave field, bottom boundary layer, and sediment transport processes throughout the entire water column. Kim et al. (2018) reported detailed model formulation of SedWaveFoam and its validation with a large wave flume experiment for sheet flow driven by monochromatic nonbreaking waves (Dohmen-Janssen and Hanes, 2002). Additional one-dimensional-vertical (1DV) SedFoam simulations (similar to an oscillating water tunnel [OWT] without a free surface) were conducted. Comparison of model results shows progressive wave streaming enhances onshore sediment transport driven by velocity skewness by about 60% for median sand grain size of 0.24 mm and velocity skewness of 0.39 (see more information in Section 4.1) that may be explained using a wave-stirring concept (Kim et al., 2018).

Sediment transport in the vicinity of a sandbar where waves shoal and break is more complicated due to the combined effects of wave velocity skewness, progressive wave streaming, and horizontal pressure gradient. The horizontal pressure gradient is important for sediment mobilization (Madsen, 1974; Sleath, 1999; Foster et al., 2006; Frank et al., 2015b) and many numerical and laboratory studies have attempted to quantify onshore sediment transport amplified by horizontal pressure gradient (or acceleration skewness) using an idealized sawtooth wave shape (Drake and Calantoni, 2001; Hsu and Hanes, 2004; Van der A et al., 2013). The Sleath parameter, S, is a ratio between the destabilizing (horizontal pressure gradient) and stabilizing forces (gravity) (Sleath, 1999). Plug flow (or momentary bed failure) was observed in OWT experiments when S was greater than 0.3. However, field observations showed that the threshold value of the magnitude of S can be as low as 0.1 in the surf zone (Foster et al., 2006), due to the combined effect of large bed shear stress and horizontal pressure gradient (Frank et al., 2015a). Cheng et al. (2017) confirm, using SedFoam, that large bed shear stress combined with large horizontal pressure gradients can trigger instabilities of the sheet flow layer and cause momentary bed failure which lowers the resulting critical S. The aforementioned studies demonstrated the importance of horizontal pressure gradient (or acceleration) in driving onshore sediment transport. However, most of the studies did not include free surface effects (Drake and Calantoni, 2001; Hsu and Hanes, 2004; Van der A et al., 2013). Full vertical profiles of cross-shore sediment transport under free surface waves can be simulated using SedWaveFoam, which allows more complete evaluation of the combined effects of progressive wave streaming, velocity skewness, and acceleration-skewness under near-breaking waves.

Sheet flow is the transport of a sediment layer with high concentration, typically driven by large bed shear stress. A near prototype-scale sandBAR SEDiment transport experiment (BARSED) was conducted in the large wave flume of O. H. Hinsdale Wave Research Laboratory at Oregon State University (Anderson et al., 2017; Mieras et al., 2017, 2019) to understand sheet flow dynamics driven by skewed-asymmetric surface waves over a fixed sandbar containing a sediment pit on the sandbar crest. Instantaneous high-resolution sediment concentration profiles, pore pressure gradients, and near-bed velocity profiles were measured concurrently (see Section 3 for more details). Maximum sheet flow layer thickness was well-correlated with maximum bed shear stress (Mieras et al., 2017). Suspended load and bed load sediment transport processes were quantified under a range of wave conditions with varying degrees of skewness and asymmetry (Mieras et al., 2019). Particularly, the measured horizontal pore pressure gradients were greater for larger acceleration skewness, and the horizontal pore pressure gradient may not be equal to the local acceleration under strongly asymmetric surface waves (Mieras et al., 2017; Anderson et al., 2017). Sediment mobilization via momentary bed failure occurred presumably due to the combined effect of large bed shear stress preceded by strong horizontal pressure gradients at flow reversal. However, flow velocity profiles within the sheet flow layer were not directly measured during BARSED, and further investigation through numerical modeling efforts is needed to understand the physical processes driving sheet flow dynamics under skewed-asymmetric surface waves.

The purpose of this study is to investigate the physical mechanisms driving sediment transport using the new numerical modeling strategy for skewed-asymmetric surface waves. SedWaveFoam is applied to simulate sheet flow driven by near-breaking waves on the sandbar crest during the BARSED experiment (Anderson et al., 2017; Mieras et al., 2017, 2019). Model formulations are discussed in Section 2. Section 3 presents the main model results including a comprehensive model validation of flow and sediment transport characteristics. Section 4 is devoted to discussion on the combined effects of progressive wave streaming, velocity skewness, and acceleration skewness. Lastly, the main conclusions of this study are summarized in Section 5.

2. Numerical models

This study uses two numerical models: SedWaveFoam (Kim et al., 2018); and SedFoam (Cheng et al., 2017). SedWaveFoam is able to concurrently resolve the surface wave field, bottom boundary layer, and sediment transport processes. SedFoam has essentially the same capabilities as SedWaveFoam in modeling sediment transport based on a two-phase flow formulation. In contrast to SedWaveFoam, however, SedFoam is only able to account for the sediment and water phases, thus it is incapable of resolving the free surface. Hence, SedWaveFoam is the primary model used in this study to investigate sheet flow driven by near-breaking waves. Free surface effects on sediment transport are isolated by comparing results from the SedWaveFoam model with SedFoam results.

2.1. Governing equations

A brief description of the numerical model is provided here with more details given elsewhere (Cheng et al., 2017; Kim, 2018; Kim et al., 2018). A Reynolds-averaged approach is adopted to avoid resolving 3D turbulence covering a wide range of scales. The Reynolds-averaged mass conservation equations for three phases (air, water, and sediment) are written as (e.g., Drew, 1983; Berberović et al., 2009)

$$\frac{\partial \phi^a}{\partial t} + \frac{\partial \phi^a u_i^a}{\partial x_i} = 0, \tag{1}$$

$$\frac{\partial \phi^w}{\partial t} + \frac{\partial \phi^w u_i^w}{\partial x_i} = 0, \tag{2}$$

$$\frac{\partial \phi^s}{\partial t} + \frac{\partial \phi^s u_i^s}{\partial x_i} = 0, \tag{3}$$

where $i = 1, 2$ for the present two-dimensional-vertical (2DV) flows and the superscripts a, w, and s represent air, water, and sediment phases, respectively. The variable ϕ stands for the volumetric concentration of each phase where the total mass conservation requires $\phi^a + \phi^w + \phi^s = 1$. The variable u_i represents the velocity of each phase. The air and water (fluid) phases are considered to be two immiscible fluids, and they are combined as the air-water mixture phase (Kim et al., 2018). Adopting the air-water interface tracking strategy of InterFoam (Berberović et al., 2009; Klostermann et al., 2012), the mass conservation equation of air-water mixture phase is expressed as

$$\frac{\partial \phi^w}{\partial t} + \frac{\partial \phi^w u_i^f}{\partial x_i} + \frac{\partial (\phi^a \phi^w u_i^r / \phi^f)}{\partial x_i} = 0, \tag{4}$$

where the relative velocity between the air and water phases, u_i^r, is obtained by iteration using the interface compression method to minimize numerical diffusion at the interface (Berberović et al., 2009; Klostermann et al., 2012). The superscript "f" stands for the mixture of air and water (fluid) phases where $\phi^a + \phi^w = \phi^f$ and $u^f = (u^a\phi^a + u^w\phi^w)/\phi^f$. In SedFoam, Eq. (4) is not incorporated and only Eqs. (2) and (3) are considered. The sediment (solid) phase is considered to be miscible with the air-water mixture (fluid) phase. Thus, the term "two-phase" henceforth refers to two miscible phases which are the air-water mixture (fluid) and sediment (solid) phases. The dynamics of both phases can be resolved by the Eulerian two-phase mass and momentum equations appropriate for sediment transport (Dong and Zhang, 1999; Li et al., 2008; Cheng et al., 2017). The Reynolds-averaged momentum equations for the present air-water mixture and sediment phases are written as (e.g., Kim et al., 2018)

$$\frac{\partial \rho^f \phi^f u_i^f}{\partial t} + \frac{\partial \rho^f \phi^f u_i^f u_j^f}{\partial x_j} = -\phi^f \frac{\partial p^f}{\partial x_i} + \rho^f \phi^f g \delta_{i2} - \sigma_t \gamma \frac{\partial \phi^a}{\partial x_i} + \frac{\partial \tau_{ij}^f}{\partial x_j} + M_i^{fs}, \tag{5}$$

$$\frac{\partial \rho^s \phi^s u_i^s}{\partial t} + \frac{\partial \rho^s \phi^s u_i^s u_j^s}{\partial x_j} = -\phi^s \frac{\partial p^f}{\partial x_i} - \frac{\partial p^s}{\partial x_i} + \rho^s \phi^s g \delta_{i2} + \frac{\partial \tau_{ij}^s}{\partial x_j} + M_i^{sf}, \tag{6}$$

where ρ^s is the sediment density ($= 2{,}650\,\mathrm{kg/m^3}$). The mixture fluid density, ρ^f, is calculated as $\rho^f = (\rho^a\phi^a + \rho^w\phi^w)/\phi^f$, in which $\rho^a = 1\,\mathrm{kg/m^3}$ and $\rho^w = 1000\,\mathrm{kg/m^3}$ here. The variable p^f is the fluid pressure, and $g = -9.8\,\mathrm{m/s^2}$ is gravitational acceleration. Since the free surface evolution is resolved, the effect of surface tension is included in the third term on the right-hand-side (RHS) of Eq. (5) where γ is the surface curvature. The surface tension coefficient σ_t is specified as $\sigma_t = 0.074\,\mathrm{kg/s^2}$ representing the air-water interface at the temperature of 20 °C. The fluid stress, τ_{ij}^f, consists of grain-scale viscous stress and turbulent Reynolds stress with the latter calculated by a two-equation k-ε turbulence model for two-phase flow (see Section 2.2.1). The particle pressure, p^s, and particle shear stress, τ_{ij}^s, are modeled with the kinetic theory of granular flow for particle collision at low to moderate concentration and phenomenological closures for enduring contact at high sediment concentration (see Section 2.2.2, and Cheng et al., 2017 for more details). The inter-phase momentum transfer between the fluid and sediment phases follows Newton's 3rd law, $M_i^{fs} = -M_i^{sf}$ which consists of drag force due to Reynolds-averaged mean velocity difference and turbulent suspension as

$$M_i^{fs} = -\phi^s \phi^f \beta (u_i^f - u_i^s) + \beta \phi^f \frac{\nu^{ft}}{\sigma_c} \frac{\partial \phi^s}{\partial x_i}, \tag{7}$$

where β is the drag parameter (Ding and Gidaspow, 1990), ν^{ft} is the turbulent viscosity of the fluid phase, and $\sigma_c = 1.0$ is the Schmidt number. More detailed formulation can be found in Cheng et al. (2017).

2.2. Closures

2.2.1. Fluid turbulence closures

Fluid stresses, τ_{ij}^f, in Eq. (5) consist of turbulent Reynolds stress, R_{ij}^{ft}, and grain-scale viscous stress, r_{ij}^f which can be written as

$$\tau_{ij}^f = R_{ij}^{ft} + r_{ij}^f = \rho^f \phi^f \left[2(\nu^{ft} + \nu^f) S_{ij}^f - \frac{2}{3} k^f \delta_{ij} \right], \tag{8}$$

in which the kinematic viscosity of carrier fluid (i.e., air-water mixture) is defined as $\nu^f = (\rho^a\phi^a\nu^a + \rho^w\phi^w\nu^w)/(\rho^a\phi^a + \rho^w\phi^w)$ where $\nu^a = 1.48 \times 10^{-5}\,\mathrm{m^2/s}$ and $\nu^w = 10^{-6}\,\mathrm{m^2/s}$. The turbulent eddy viscosity, ν^{ft}, is calculated by turbulent kinetic energy (TKE), k^f, and turbulent dissipation rate, ε^f, as $\nu^{ft} = C_\mu (k^f)^2/\varepsilon^f$ where C_μ is an empirical coefficient ($C_\mu = 0.09$). The deviatoric part of the strain rate of mixture fluid phase, S_{ij}^f, is defined as $S_{ij}^f = \frac{1}{2}\left(\frac{\partial u_i^f}{\partial x_j} + \frac{\partial u_j^f}{\partial x_i}\right) - \frac{1}{3}\frac{\partial u_k^f}{\partial x_k}\delta_{ij}$.

The balance equation for TKE is written as (Kim et al., 2018)

$$\frac{\partial \rho^f k^f}{\partial t} + \frac{\partial \rho^f u_j^f k^f}{\partial x_j} = R_{ij}^{ft} \frac{\partial u_i^f}{\partial x_j} + \frac{\partial}{\partial x_j}\left[\rho^f \left(\nu^f + \frac{\nu^{ft}}{\sigma_k} \right) \frac{\partial k^f}{\partial x_j} \right] - \rho^f \varepsilon^f - \frac{2\beta(1-\alpha)\phi^s k^f}{\phi^f} - \frac{\rho^f \nu^{ft}}{\phi^f \sigma_c} \frac{\partial \phi^s}{\partial x_j}(s-1) g \delta_{j2}, \tag{9}$$

where $\sigma_k = 1.0$ is the Schmidt number for TKE (Rodi, 1993), and $s = \rho^s/\rho^f$ is the specific gravity of sediment. The TKE attenuation due to particle inertia effects is included in the fourth term on the RHS of Eq. (9) following Cheng et al. (2017). Particularly, the level of correlation between fluid and sediment velocity fluctuations is modeled as $\alpha = \exp(-BS_t)$ following Danon et al. (1977) and Chen and Wood (1985), in which $B = 0.16$ is an empirical coefficient and S_t is the Stokes number modeled by particle response time and characteristic time scale of energetic eddies. The buoyancy effect caused by density stratification is also included in the last term of Eq. (9). For sediment transport, this term usually contributes as an attenuation term of TKE due to stable density stratification.

Similarly, the balance equation for turbulence dissipation rate is written as

$$\frac{\partial \rho^f \varepsilon^f}{\partial t} + \frac{\partial \rho^f u_j^f \varepsilon^f}{\partial x_j} = C_{1\varepsilon} R_{ij}^{ft} \frac{\varepsilon^f}{k^f} \frac{\partial u_i^f}{\partial x_j} + \frac{\partial}{\partial x_j}\left[\rho^f \left(\nu^f + \frac{\nu^{ft}}{\sigma_\varepsilon} \right) \frac{\partial \varepsilon^f}{\partial x_j} \right] - C_{2\varepsilon} \rho^f \frac{\varepsilon^f}{k^f} \varepsilon^f - C_{3\varepsilon} \frac{\varepsilon^f}{k^f} \frac{2\beta(1-\alpha)\phi^s k^f}{\phi^f} - C_{4\varepsilon} \frac{\varepsilon^f}{k^f} \frac{\rho^f \nu^{ft}}{\phi^f \sigma_c} \frac{\partial \phi^s}{\partial x_j}(s-1) g \delta_{j2}, \tag{10}$$

where the empirical coefficients are selected as $C_{1\varepsilon} = 1.44$, $C_{2\varepsilon} = 1.92$, $C_{3\varepsilon} = 1.2$, and $\sigma_\varepsilon = 1.0$ (Rodi, 1993; Cheng et al., 2017). Similar to Eq. (9), the damping effect due to particle inertia and buoyancy effect due to the density stratification are included in the fourth and last terms on the RHS of Eq. (10). The empirical coefficient $C_{4\varepsilon}$ is defined as $C_{4\varepsilon} = 0$ for stable density stratification while it is automatically adjusted to $C_{4\varepsilon} = 1$ for an unstable stratified condition.

2.2.2. Particle stress closures

The particle stresses due to intergranular interactions can be generated by intermittent collision and enduring contact/frictional forces. The particle pressure, p^s, and shear stress, τ_{ij}^s, are modeled as consisting of a collisional component (superscript "sc") and a frictional contact component (superscript "sf") (e.g., Hsu et al., 2004):

$$p^s = p^{sc} + p^{sf}, \tag{11}$$

$$\tau_{ij}^s = \tau_{ij}^{sc} + \tau_{ij}^{sf}. \tag{12}$$

The collisional component of particle pressure, p^{sc}, and particle shear stress, τ^{sc}, are modeled through the granular temperature obtained from the kinetic theory of granular flow (Jenkins and Savage, 1983; Ding and Gidaspow, 1990). The granular temperature accounts for advection, diffusion, shear production, and dissipation caused by inelastic collision and particle-induced fluctuations (Ding and Gidaspow, 1990; Cheng et al., 2017). Where sediment concentration is high enough, intermittent particle collisions rarely occur, and the modeled granular temperature decreases. In such a dense mobile sediment layer, the frictional contact component becomes the dominant contribution to the particle pressure and particle shear stress. The frictional contact components of particle pressure, p^{sf}, and particle shear stress, τ^{sf}, are modeled following Johnson and Jackson (1987) and Gidaspow (1994), respectively. The threshold values are specified as $\phi^{sf} = 0.57$ where the variable ϕ^{sf} represents the threshold concentration where enduring contact becomes dominant. More detailed formulation is provided in Cheng et al. (2017).

3. Results

3.1. Experimental setup

In BARSED, a fixed, scaled down barred beach profile was

constructed based on an observed beach profile during the Duck94 experiment (Garcez Faria et al., 1996; Gallagher et al., 1998; Scott et al., 2005), with a sediment pit installed on the sandbar crest. The wave flume has an overall length of 104 m, width of 3.7 m, and depth of 4.6 m. The still water depth during tests was 2.448 m at the wave maker and 1.001 m at the sandbar crest. The sediment pit dimensions were 3.66 × 3.66 × 0.17 m (length × width × depth), and it was filled with sediment of median grain diameter, $d_{50} = 0.17$ mm ($d_{10} = 0.08$ mm and $d_{90} = 0.27$ mm) and specific gravity of $s = 2.65$.

An array of sensors was positioned over the sandbar crest to measure velocity and sediment concentration profiles in the sheet flow and suspended load layers. The velocity profile was measured with a vertical array of six acoustic Doppler velocimeters (ADVs; 100 Hz) spanning the water column from 0.1 m to 1.1 m above the initial sediment bed level with a vertical spacing of 0.2 m. Near-bed velocity profiles up to 0.021 m above the sediment bed at 0.001 m resolution were measured using acoustic Doppler profiling velocimeters (ADPVs; 100 Hz). Suspended sediment concentration profiles were measured in the lower half of the still water column with dual-array fiber optic backscatter sensors (FOBS; 8 Hz) with a vertical resolution ranging from 0.01 to 0.07 m, and near-bed sediment concentration profiles were measured using conductivity concentration profilers (CCPs; 8 HZ) (Lanckriet et al., 2013) yielding ϕ^s up to 0.02 m above the sediment bed with a vertical resolution of 0.001 m. In addition, the cross-shore and vertical pore pressure gradients were obtained from an array of buried pore pressure transducers (100 Hz). Free surface elevation was observed at the cross-shore center of the sediment pit with a pressure gauge, p_0, positioned a few centimeters above the sediment bed. The cross-shore variation of free surface elevation was measured using 11 twin-wire capacitance wave gauges and 6 ultrasonic wave gauges with a sampling rate of 100 Hz.

In BARSED, each trial consisted of generating 10 monochromatic waves, with ramp up and ramp down phases at the start and end of each trial. Flow velocity and sediment concentration data were separated into individual wave events based on zero up-crossings of $p_0(t)$. Model validation and further discussion will be conducted using observations from case S1T7H60 (Mieras et al., 2018), which is composed of data from three separate trials containing 29 waves in total (Mieras et al., 2019). A monochromatic wave train with wave period (T) of 7.0 s and wave heights of 0.60 m was generated at the wave maker, and subsequently shoaled to 0.94 m at the sandbar crest (Anderson et al., 2017; Mieras et al., 2017, 2019). For a trial $T = 7.0$ s, roughly three waves were present within the 20 s ramp up phase. Thus, the first three waves in the signal for each trial of S1T7H60 correspond to the ramp up phase were ignored in the zero up-crossing analysis. Additional details about the experimental setup, wave conditions, and data analysis are provided in Anderson et al. (2017) and Mieras et al. (2017, 2019).

3.2. Numerical model

A 2DV numerical model domain (Fig. 1) was created assuming the homogeneity of turbulent flow statistics in the spanwise direction (y). The positive x-direction is denoted as the wave propagation direction and $x = 0$ is defined at the cross-shore center of the sediment pit. The z-coordinate (vertical) is defined as positive upward and $z = 0$ is located at the top of initial sediment bed level, 1.001 m below the initial still water level. The mesh was first generated with uniform grids of 16 mm in width and 8 mm in height. Near the two ends of the sandbar crest, non-rectangular grids were used to resolve sharp bathymetry gradients. The grids near the edges of the sediment pit were refined with three layers of unstructured triangular meshes using the snappyHexMesh tool (Fig. 1a) (Jackson, 2012). As a result, the sediment pit was shortened by 0.55 m from each side so that only rectangular grids were used to resolve high concentration sheet flow transport with a final grid size of 2 mm (width) and 1 mm (height). A total number of 4.6 million grid points were used. The resulting sediment pit length in the numerical model is 2.56 m (compared with the experimental pit length of 3.66 m), which is shown later to be sufficiently long to preserve a quasi-equilibrium region in the streamwise direction.

The numerical wave flume geometry is identical to the physical experiment, except a relaxation zone of one wave length (Jacobsen et al., 2012) was added at the inlet ($x = -79.26$ m to $x = -45.14$ m) to mimic the wave maker and its active wave absorption capability (Fig. 1b–c). In the numerical model, a 50th order stream function was used to generate monochromatic waves, consistent with the physical experiment. For the immobile concrete beach profile, a wall boundary with no-flux boundary condition was applied for scalar quantities. For velocities, the wall-normal component was specified to be zero and a no-slip boundary condition was applied to the wall-parallel component. Atmospheric and empty boundary conditions of OpenFOAM were adopted for the top boundary and two lateral boundaries, respectively.

The spatial and temporal evolution of sediment transport driven by surface waves over the sandbar crest are shown in Fig. 2. The spatial evolution is presented as an $x - z$ plane snapshot of volumetric sediment concentration (ϕ^s) in the sediment pit at $t = 59$ s with fluid velocity (u_i^f) vectors overlaid (Fig. 2a). The instantaneous location of immobile bed location (defined as the elevation where $|u^s| < 10^{-4}$ m/s) is denoted by the dashed curve. Scour and accumulation of sediment was observed at the upstream and downstream edges of the sediment pit, respectively, due to net onshore sediment transport driven by the surface waves. However, the central region of the sediment pit far enough from these edge effects, where the range of -0.42 m$< x < 0.35$ m (a span of 0.77 m) was found to yield a region where wave-averaged flow velocity and sediment concentration are homogeneous in the x-direction, i.e., quasi-equilibrium in the x-direction. For instance, the index of agreements (Willmott, 1981; Willmott and Wicks, 1980), IA, of the vertical profiles of wave-averaged sediment flux were greater than 0.999. Moreover, the orbital excursion amplitude was roughly 1 m in this case (Mieras et al., 2017); hence, advection of suspended sediment from the transitions at the offshore/onshore flanks unlikely impacted the central region of the sandbar crest. Thus, flow and sediment transport quantities are in quasi-equilibrium in the streamwise direction for this 0.77 m long span, and the shortened sediment pit length in the model plays a negligible role when examining model results in the middle of the sediment pit ($x = 0$).

The temporal evolution of ϕ^s up to the seventh wave at $x = 0$ is shown in Fig. 2b. An investigation of Reynolds-averaged numerical model results suggests that the vertical profiles of wave-averaged sediment fluxes are qualitatively similar among the fifth to seventh waves ($IA > 0.934$) after a vertical coordinate shift (see Section 3.3.2) to account for lowered sediment bed level due to net onshore sediment transport.

It should be pointed out that an unrealistically large TKE can develop beneath surface waves using the standard k-ε (and other two equation) turbulence models, as shown by several previous studies (Brown et al., 2016; Devolder et al., 2017; Larsen and Fuhrman, 2018). Larsen and Fuhrman (2018) showed that this problem is not restricted to the near-surface region, and is rather due to the unconditional instability of two equation closure models in the nearly-potential flow region beneath surface waves. However, our numerical experiments suggest the over-predicted TKE, which grows fastest at the free surface (see Eq. 2.12 in Larsen and Fuhrman, 2018), does not impact the sediment bed for the present study (Kim, 2018), which focuses on the analysis under the seventh waves (between two black dotted lines in Fig. 2b). A formally stable turbulence model, making use of the modified eddy viscosity approach as shown by Larsen and Fuhrman (2018), will be incorporated in a future extension of SedWaveFoam.

3.3. Model validations

The measured data were obtained from three repeated trials, so that the development of undertow and the effect of decreasing/increasing

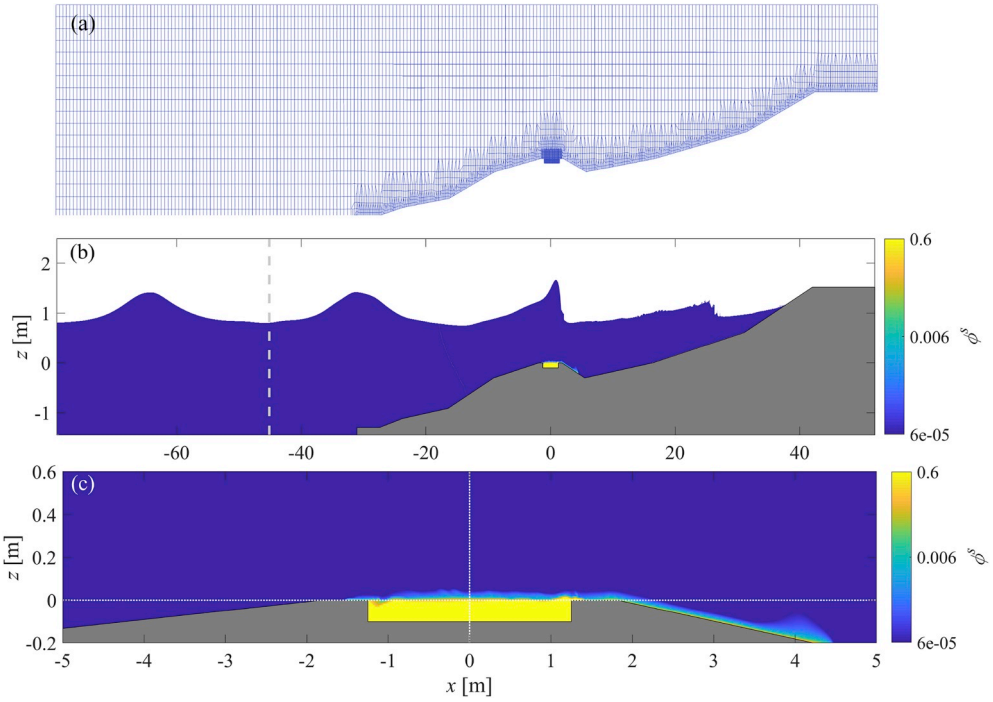

Fig. 1. The numerical wave flume with (a) mesh, (b) view of the entire flume, and (c) zoomed in view near the sandbar crest at $t = 59$ s. Different colors in (b) and (c) represent air (white), water (blue), and sediment (yellow to blue represents volumetric concentration, see color bar) phases. For visibility, the mesh in (a) is down-sampled by 35 times in each direction and vertical scale is stretched by seven times. The vertical gray dashed line at $x = -45.14$ m in (b) represents the exact boundary of the inlet relaxation zone ($x < -45.14$ m). (For interpretation of the references to color in this figure legend, the reader is referred to the Web version of this article.)

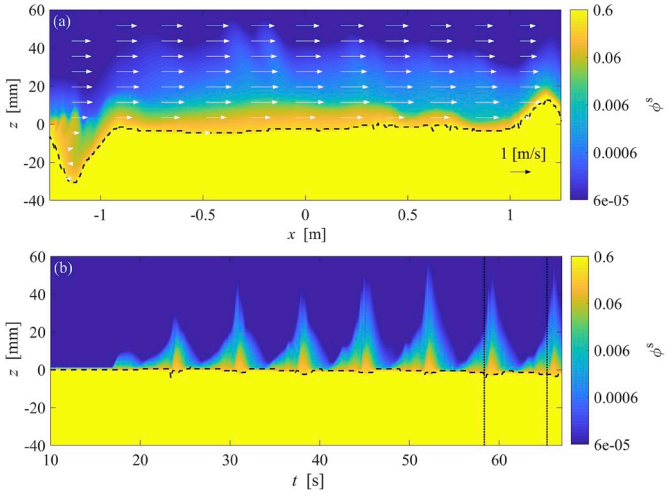

Fig. 2. The snapshots of (a) sediment concentration ϕ^s over the entire sediment pit at $t = 59$ s where vectors represent fluid velocity u_i^f. Panel (b) shows temporal evolution of ϕ^s at the center of the sediment pit ($x = 0$) where ϕ^s between two black dotted vertical lines is under seventh wave. The black dashed curves in (a) and (b) represent the immobile bed location.

sediment bed level change at the sandbar crest due to net sediment transport were minimized. The measured data obtained from the last ten waves (fourth to 13th waves) of each trial were used to calculate the phase-averaged (or ensemble-averaged) quantities and numerical model validation is conducted with these averaged measured data (Mieras et al., 2017, 2019).

3.3.1. Flow characteristics

Fig. 3 shows the model-data comparison of free surface elevation (η) at four selected cross-shore locations, where the instantaneous measured η was averaged across the three trials. In carrying out model versus measured data validation, the ramp up portion of the signal ($t \leq 30$ s) was ignored because of different wave generation methods between the physical experiment and numerical model. For the model validation, *IA* and normalized-root-mean-square errors (NRMSE) are used to represent the similarity of trend and the mean of squared errors with reference to the range of measured data, respectively. The overall agreement between measured and modeled η was *IA* = 0.995, 0.936, 0.941, 0.936 at $x = -27.41$ m, -1.93 m, 1.73 m, 16.37 m, respectively. The NRMSEs normalized by maximum measured wave height at each location were 4.8%, 8.1%, 11.2%, 10.2%. In general, a better agreement was obtained at the locations seaward of the sandbar crest. However, the model was able to capture highly skewed and asymmetric near-breaking and broken waves over the sandbar. Recorded visual observation from the physical experiment indicated waves broke about 1 m landward of the center of the sediment pit matching present model results. Hence, the sediment transport near the center of the sediment pit is driven by highly skewed and asymmetric near-breaking waves and wave breaking turbulence is unlikely to affect near-bed sediment transport in this case (Kim, 2018).

The two main components of fluid velocity (streamwise: u^f and vertical: w^f) at the center of the sediment pit are shown at three selected vertical locations in Fig. 4, coinciding with the elevations of three ADVs from the experimental study. Reynolds-averaged model results for the seventh wave (black curves in Fig. 4) are compared with phase-averaged measured data (gray curves in Fig. 4). The model was able to predict velocities u^f (w^f) with *IA* of 0.997, 0.997, 0.996 (0.978, 0.986, 0.968) and NRMSE (normalized by measured $u^f_{\max}$ or $w^f_{\max}$) of 5.7%, 5.7%, 6.4% (12.7%, 7.1%, 5.1%) at $z = 0.516$ m, 0.315 m, and 0.121 m, respectively. In both experimental observations and model results, u^f has a similar magnitude at different vertical locations (left column) while the magnitude of w^f is reduced by 61.2% on average approaching the sediment bed (right column).

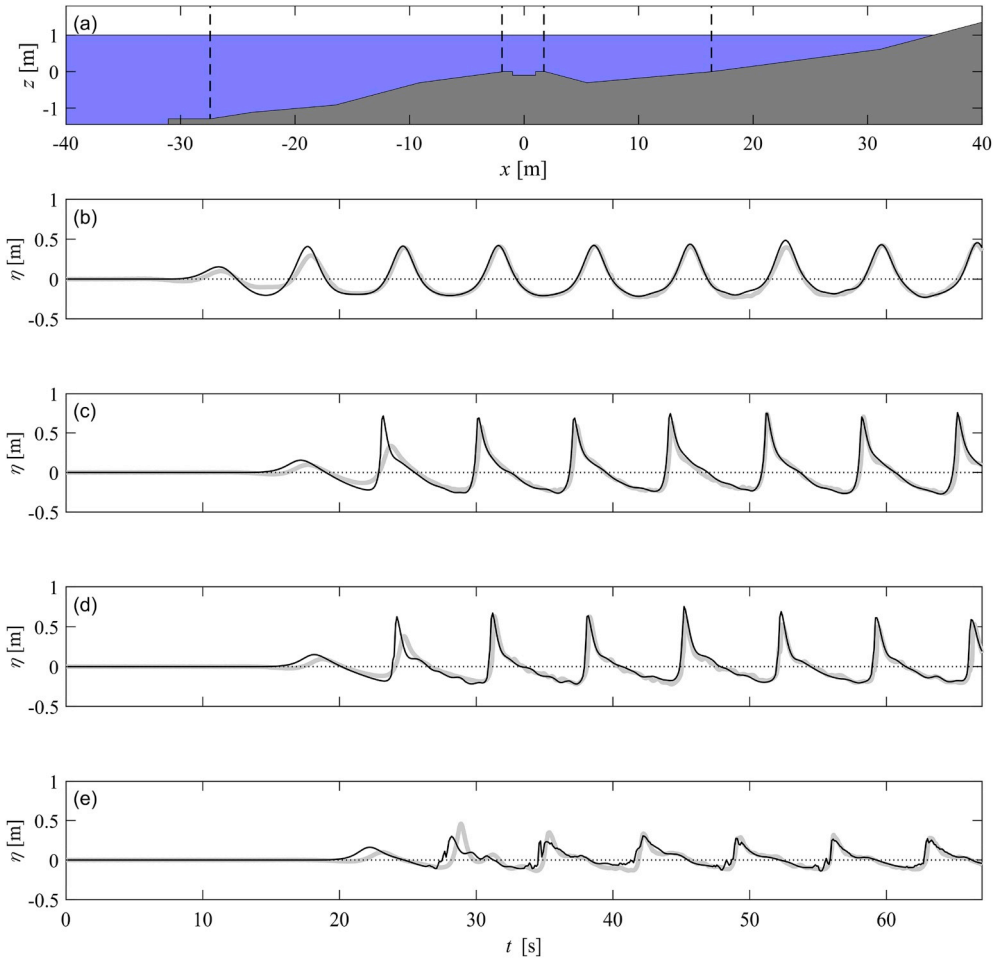

Fig. 3. (a) A schematic of wave gauge locations in the flume denoted by dashed vertical lines and the free surface elevation for measured data averaged over three trials (thick gray curves) and model results (thin black curves) at (b) $x = -27.41$ m, (c) $x = -1.93$ m, (d) $x = 1.73$ m, and (e) $x = 16.37$ m, as indicated in (a).

3.3.2. Wave bottom boundary layer and sediment transport

The sediment bed level associated with each wave was slightly different due to non-zero net sediment transport. Hence, a local vertical coordinate system for each wave (ensemble) was introduced in Mieras et al. (2017, 2019) to ensure the vertical profiles are referenced to the same local initial sediment bed level for phase-averaging. The inflection point of ϕ^s, i.e., $\partial^2\phi^s/\partial z^{*2} = 0$, was identified based on fitting a curve to the sediment concentration profiles following O'Donoghue and Wright (2004a), and defining $z^* = 0$ as the elevation of the inflection point at $t/T = 0$ for each ensemble. The same approach was applied to the model results for consistency. The sediment bed level decreased from $z = -2.2$ mm to -3.4 mm in the model results, from the fourth to the seventh wave (see Fig. 2b).

The modeled time series of u^f at $z^* = 30$ mm above the sediment bed agrees well with measured data ($IA = 0.998$ and NRMSE = 3.8% in Fig. 5a). In the present case, the maximum modeled wave bottom boundary layer (WBBL) thickness was about 30 mm (see Section 4.1); hence u^f at $z^* = 30$ mm is hereafter considered as the free-stream velocity, u^f_∞. At the free-stream, modeled (measured) velocity skewness was $R = 0.61$ (0.65) and $Sk_u = 0.38$ (0.58) where the quantities are defined as $R = u^f_{\infty,\max}/(u^f_{\infty,\max} - u^f_{\infty,\min})$ (e.g., Watanabe and Sato, 2004) and $Sk_u = \langle (u^f_\infty)^3\rangle/\langle (u^f_\infty)^2\rangle^{3/2}$, in which $\langle\rangle$ represents the wave-average operator. Similarly, acceleration skewness can be quantified through $\beta = \dot{u}^f_{\infty,\max}/(\dot{u}^f_{\infty,\max} - \dot{u}^f_{\infty,\min})$ (e.g., Van der A et al., 2013) where $\dot{u}^f_\infty = \partial u^f_\infty/\partial t$ and $Sk_a = \langle (\dot{u}^f_\infty)^3\rangle/\langle (\dot{u}^f_\infty)^2\rangle^{3/2}$ (e.g., Drake and Calantoni, 2001). At $z^* = 30$ mm, $\beta = 0.73$ (0.67) and $Sk_a = 2.31$ (2.18) were obtained for model results (measured data). The numerical model was able to reproduce important higher order flow statistics relevant to sediment transport. Moreover, it is expected that sediment transport in this case is driven by both highly velocity-skewed and acceleration-skewed waves (see Table 1).

Vertical profiles of u^f at the center of the sediment pit at several instants are also compared (Fig. 5b–i). In the physical experiment, velocities in the high sediment concentration sheet flow layer could not be measured due the attenuation of high frequency acoustic signal from the ADPV. Velocities observed within the sheet flow layer were subsequently discarded following Mieras et al. (2019). The agreement of u^f profiles when high local acceleration occurs (i.e., $\partial u^f/\partial t > 2$ m/s^2, Fig. 5a) are less satisfactory due to overpredicted overshoot of u^f at $t/T = 0.014$ (NRMSE = 46.4%, Fig. 5b) and $t/T = 0.043$ (NRMSE = 15.7%, Fig. 5c). At other instants, the model is able to predict u^f profiles well, with NRMSE = 11.3%, 12.3%, 4.7%, 11.6%, and 6.5% at $t/T = 0.086$, 0.257, 0.657, 0.886, and 0.943, respectively (see Fig. 5d, e, g, h, i).

Fig. 6 shows model-data comparison of near-bed TKE at eight different instants. A high-pass filter with a selected cutoff frequency was applied to $\tilde{u}_i^f(t/T, z^*)$ for each ensemble (an ensemble is defined as an individual wave, where the fourth through the 13th waves in each trial, with three total trials, yielded 29 ensembles) using the Butterworth filter for the measured data, in which $\tilde{}$ represents the demeaned quantity where $u_i^f(t/T, z^*) = \langle u_i^f(z^*)\rangle + \tilde{u}_i^f(t/T, z^*)$, to extract turbulent velocity fluctuations, $\tilde{u}_i^{f'}(t/T, z^*)$, while excluding the influence of evolving currents, waves, and long waves in the wave flume. The magnitude of measured TKE is slightly sensitive to the chosen cutoff frequency (Fig. 6). Thus, measured TKE was calculated with three

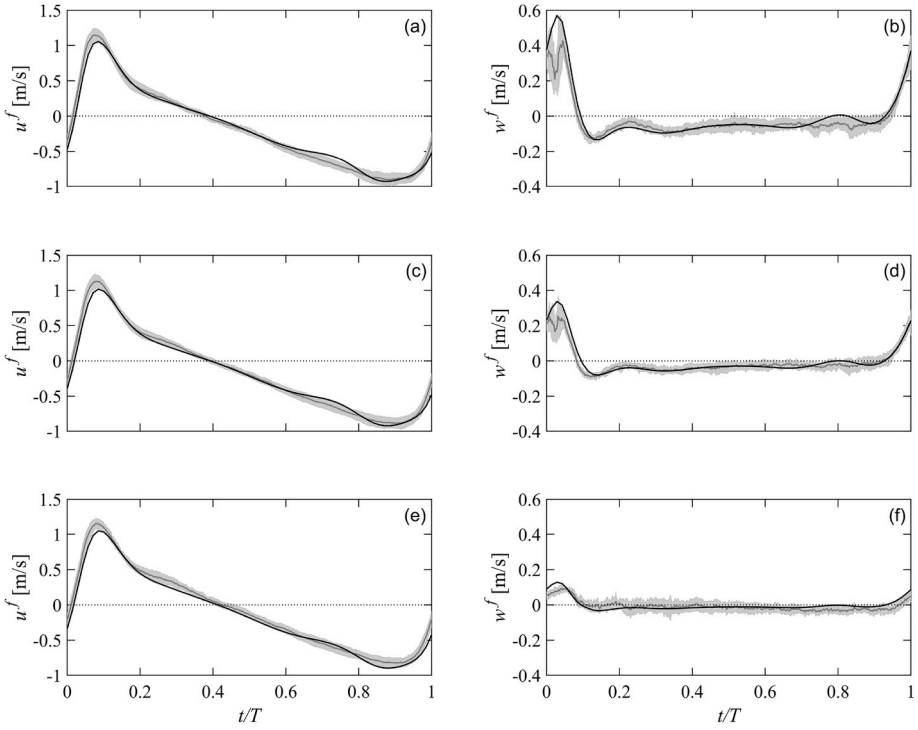

Fig. 4. The (a,c,e) u^f and (b,d,f) w^f time series for measured data (gray curves, phase-averaged; gray envelopes, ± 1 standard deviation) and model results (black curves) at $x = 0$ and three vertical elevations at (a,b) $z = 0.516$ m, (c,d) $z = 0.315$ m, and (e,f) $z = 0.121$ m.

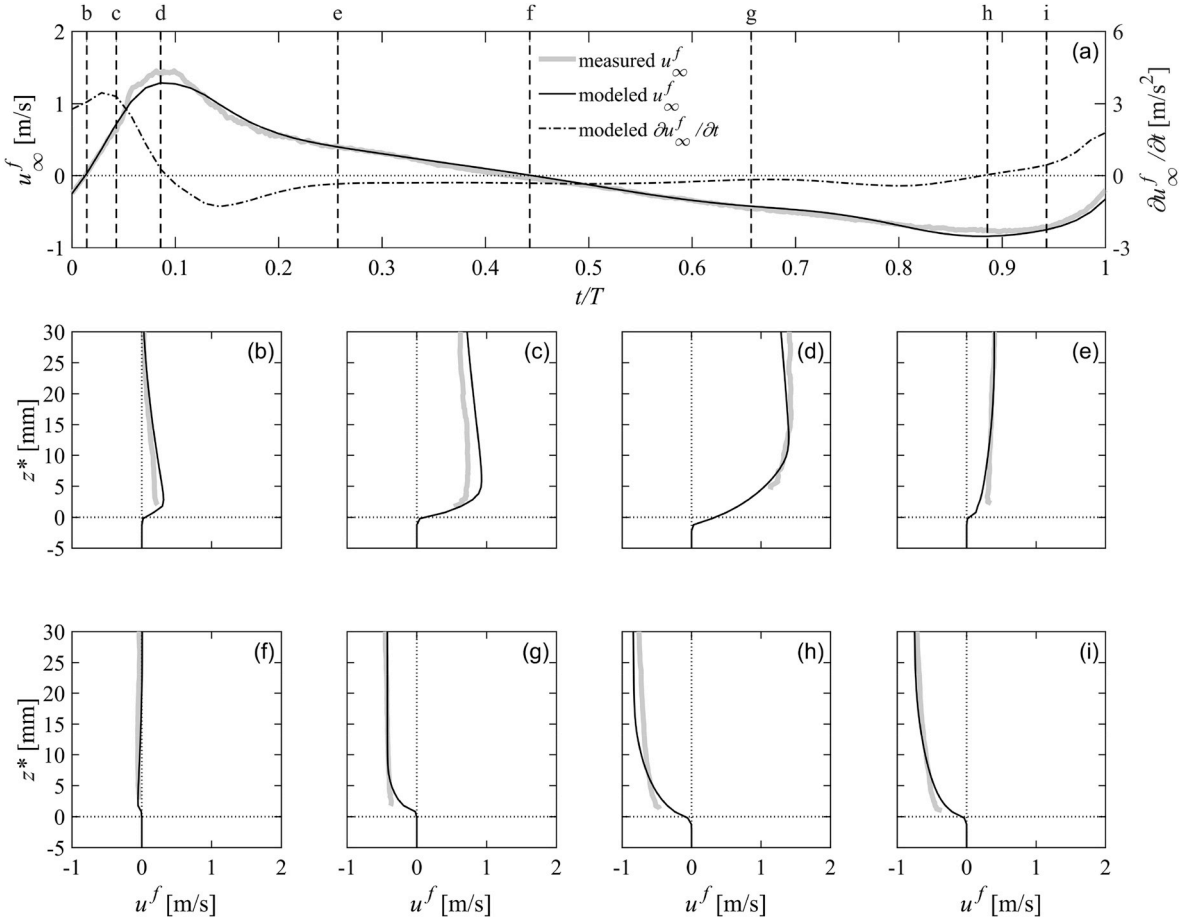

Fig. 5. (a) Time series of measured u^f_∞ (gray curves), modeled u^f_∞ (black solid curves), and modeled $\partial u^f_\infty/\partial t$ (black dash-dotted curve) at $x = 0$. (b) – (i) are vertical profiles of u^f at (b) $t/T = 0.014$, (c) $t/T = 0.043$, (d) $t/T = 0.086$, (e) $t/T = 0.257$, (f) $t/T = 0.443$, (g) $t/T = 0.657$, (h) $t/T = 0.886$, (i) $t/T = 0.943$, as marked in (a) using vertical dashed lines.

Table 1
Key sediment transport quantities of present study compared with those under nonbreaking waves.

ID	Sheet flow under near- breaking waves (Present study)	Sheet flow under nonbreaking waves (Kim et al., 2018)
d_{50}	0.17 mm	0.24 mm
H at the sediment pit	0.94 m	1.55 m
T at the sediment pit	7.0 s	6.5 s
h at the sediment pit	1.001 m	3.5 m
R of SedWaveFoam	0.61	0.62
Sk_u of SedWaveFoam	0.38	0.39
β of SedWaveFoam	0.73	0.49
Sk_a of SedWaveFoam	2.31	−0.07
$\langle u^f_{\mathrm{diff}} \rangle_{\max}$	5.6 cm/s	4.4 cm/s
u^f_{RMS}	0.31 m/s	0.64 m/s
$\Theta_{\max}$ of SedWaveFoam (SedFoam) at the center of sediment pit	3.11 (2.45)	1.58 (1.41)
$\lvert S_{\max} \rvert$ of SedWaveFoam (SedFoam) at the center of sediment pit	0.18 (0.19)	0.07 (0.08)
$\delta_{s,\max}$ of SedWaveFoam (SedFoam)	10.01 mm (7.00 mm)	6.25 mm (5.72 mm)
$\langle q^s \rangle$ of SedWaveFoam (SedFoam)	102.58 mm^2/s(29.63 mm^2/s)	80.27 mm^2/s(50.36 mm^2/s)

different cutoff frequencies (i.e., 0.5 Hz, 1 Hz, and 2 Hz) as

$$k^f(t/T, z^*) = \frac{\overline{\tilde{u}^{f}_{i}{}'(t/T, z^*) \cdot \tilde{u}^{f}_{i}{}'(t/T, z^*)}}{2}, \tag{13}$$

in which $i = 1,\ 2,\ 3$ and "$\bar{\ }$" represents the ensemble-average operator for the measured data. In SedWaveFoam, TKE was directly computed from the RANS model (Eq. (9)). Regardless of the uncertainties in the choice of cutoff frequency, the qualitative agreements between measured data and model results are very good. Quantitative comparisons between measured and modeled TKE are made using a cutoff frequency of 1 Hz, suggested by a previous study using the same large wave flume with similar bathymetry and instrumentation (Scott et al., 2005). In general, the magnitude of modeled TKE under the seventh wave agreed well with the measured data. Using 1 Hz as the cutoff frequency, we obtained NRMSE = 40.0% (Fig. 6c), 38.6% (Fig. 6d), 31.4% (Fig. 6e) under the wave crest, and 28.6% (Fig. 6g), 59.7%

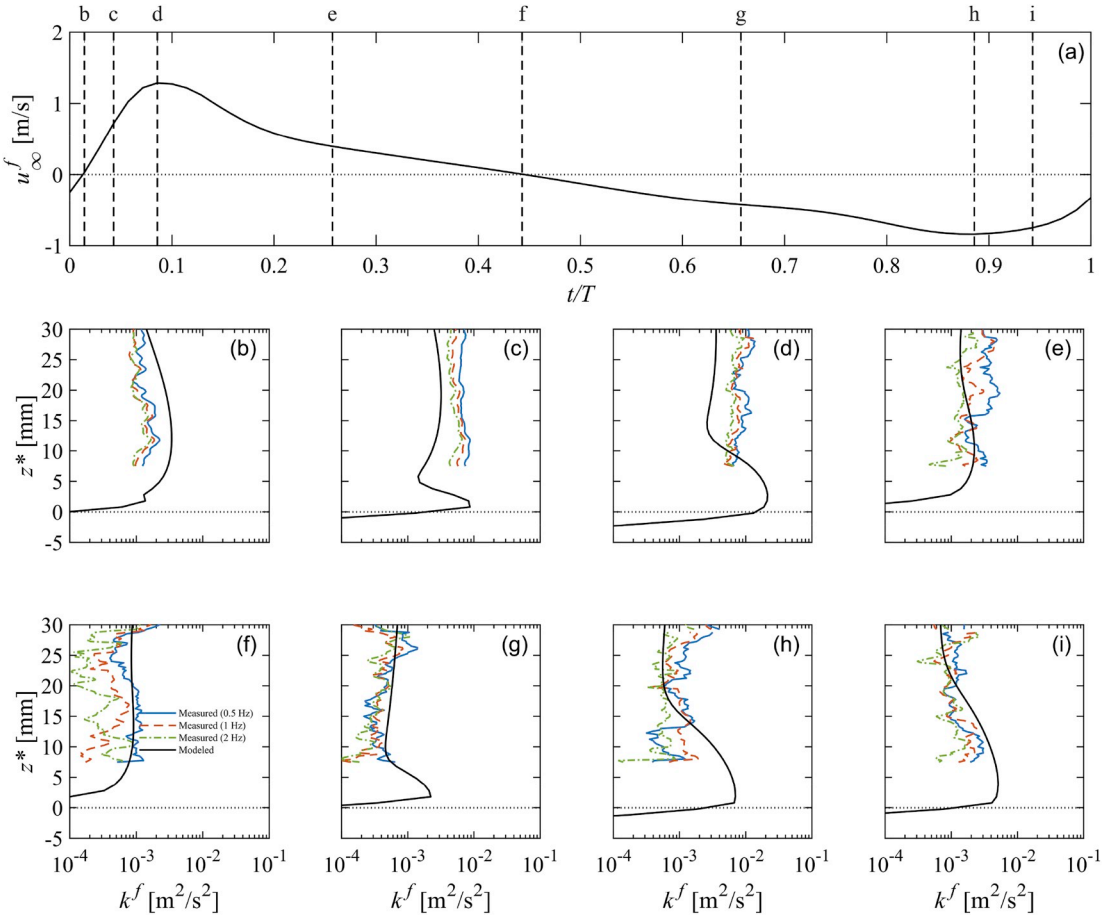

Fig. 6. (a) Time series of modeled u^f_∞ at $x = 0$. (b) – (i) are measured (blue solid curves, cutoff frequency of 0.5 Hz; red dashed curves, cutoff frequency of 1 Hz; green dash-dotted curves, cutoff frequency of 2 Hz) and modeled (black curves) vertical profiles of k^f at (b) $t/T = 0.014$, (c) $t/T = 0.043$, (d) $t/T = 0.086$, (e) $t/T = 0.257$, (f) $t/T = 0.443$, (g) $t/T = 0.657$, (h) $t/T = 0.886$, (i) $t/T = 0.943$, as marked in (a) using vertical dashed lines. (For interpretation of the references to color in this figure legend, the reader is referred to the Web version of this article.)

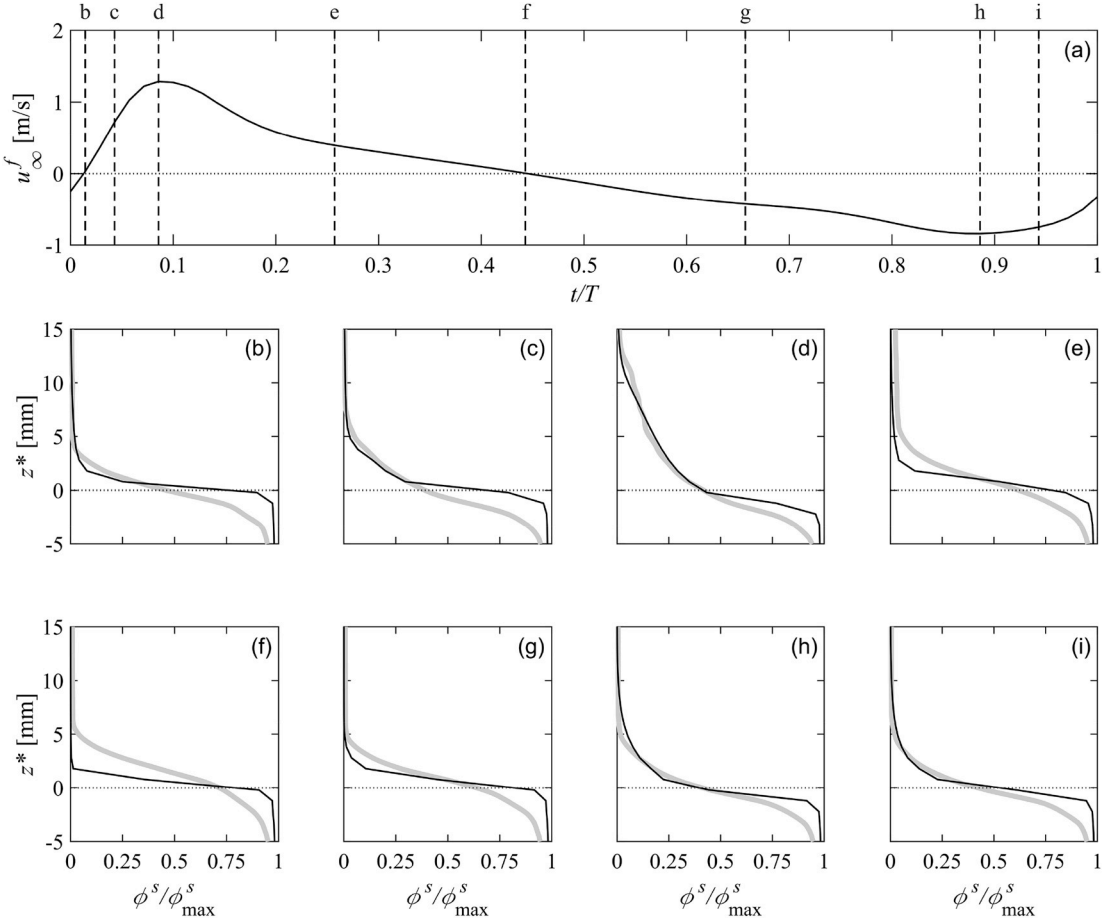

Fig. 7. (a) Time series of modeled u_∞^f at $x = 0$. (b) – (i) are measured (gray curves) and modeled (black curves) vertical profiles of ϕ^s/ϕ^s_{max} at (b) $t/T = 0.014$, (c) $t/T = 0.043$, (d) $t/T = 0.086$, (e) $t/T = 0.257$, (f) $t/T = 0.443$, (g) $t/T = 0.657$, (h) $t/T = 0.886$, (i) $t/T = 0.943$ on a linear scale.

(Fig. 6h), 43.3% (Fig. 6i) under wave trough. Generally, the near-bed TKE is on the order of O(10^{-3}~10^{-2}) m^2/s^2 under wave crest while it is reduced to O(10^{-3}) m^2/s^2 during flow reversal (Fig. 6b and f). In particular, very close to the sediment bed in the sheet flow layer ($z^* < 6$ mm), model results suggest a rapid increase of TKE during the acceleration phase (Fig. 6c, d, g, h) by almost an order of magnitude larger compared with that above the sheet flow layer.

Vertical profiles of normalized volumetric sediment concentration ($\phi^s/\phi^s_{\max}$) are compared at the same eight instants as before (Fig. 7b – 7i in linear plots and 8b – 8i in semi-log plots with a wider y axis). The agreements between measured and modeled $\phi^s/\phi^s_{\max}$ profiles were good ($IA = 0.992$, 0.995 and NRMSE = 5.6%, 4.5% at $t/T = 0.086$ and 0.886, respectively) under the wave crest (Fig. 7d) and trough (Fig. 7h). Discrepancies in the higher concentration region during flow reversal (Fig. 7b and f) may be due to the fact that the CCP sensor (covering $\phi^s/\phi^s_{\max} > 0.03$) used in the physical experiment to estimate sediment concentration tends to smooth out the concentration profile at the so-called shoulder ($IA = 0.990$, 0.992 and NRMSE = 6.5%, 5.8% at $t/T = 0.014$ and 0.443, respectively). The minimum sheet flow layer thickness that can be resolved by the CCP is about 5 mm (Lanckriet et al., 2014) while the model results suggest that the sheet flow layer thickness can be as small as 1 mm during onshore-to-offshore flow reversal (see more discussion later). Notable discrepancy is observed in the very dilute region ($\phi^s/\phi^s_{\max} < 0.01$) in the semi-log plots (Fig. 8). The measured data exhibited a nearly uniform sediment concentration profile ($\phi^s/\phi^s_{\max} \approx 0.01$) which might be attributed to wash load and uncertainties in calibration of sensors. Thus, the contribution of sediment flux in the dilute region is excluded in the following sediment transport rate comparison for both measured and modeled data. In the model results, the contribution of very dilute region to sediment transport rate was less than 5.5% on average. Overall, SedWaveFoam can reproduce the general shape of the volumetric sediment concentration profile (Figs. 7 and 8).

The temporal evolution of sheet flow layer thickness (δ_s), and sediment transport rate (q^s) with reference to the time series of u^f are shown in Fig. 9. The instantaneous elevation of the top of sheet flow layer (z_s^*) is defined at the vertical location of $\phi^s = 0.08$ (Dohmen-Janssen et al., 2001; Ribberink et al., 2008). The instantaneous sediment bed location (z^*_{bed}) of model results is defined where streamwise sediment velocity, u^s, is smaller than a threshold value, $|u^s| < 5 \times 10^{-4}$ m/s, representing a nearly immobile bed. The sheet flow layer thickness, δ_s, is defined as $\delta_s = z_s^* - z^*_{\text{bed}}$. In the measured data, z^*_{bed} was estimated as the elevation of the intersection between a straight line extended outward from the inflection point of $\phi^s(z^*)$ following the slope based on a composite power law profile, and a vertical straight line through $\phi^s_{\max}$ (Mieras et al., 2017). Due to the aforementioned smoothing effect from the CCP, measured δ_s can be over-predicted, and requires a correction formula to obtain the true δ_s (Lanckriet et al., 2014). The modeled δ_s was close to the measured δ_s where $IA = 0.876$ and NRMSE = 19.1%. The maximum sheet flow layer thickness ($\delta_{s,\max}$) was about 10 mm in this case.

As pointed out before, velocity profiles in the sheet flow layer were not directly measured during the physical experiment. However, velocity information is critical in estimating the time-dependent sediment transport rate, q^s, using the measured sediment concentration data. In the sheet flow layer, u^s was approximated by extrapolating the measured velocity at z_s^* down to zero at z^*_{bed} (Mieras et al., 2019):

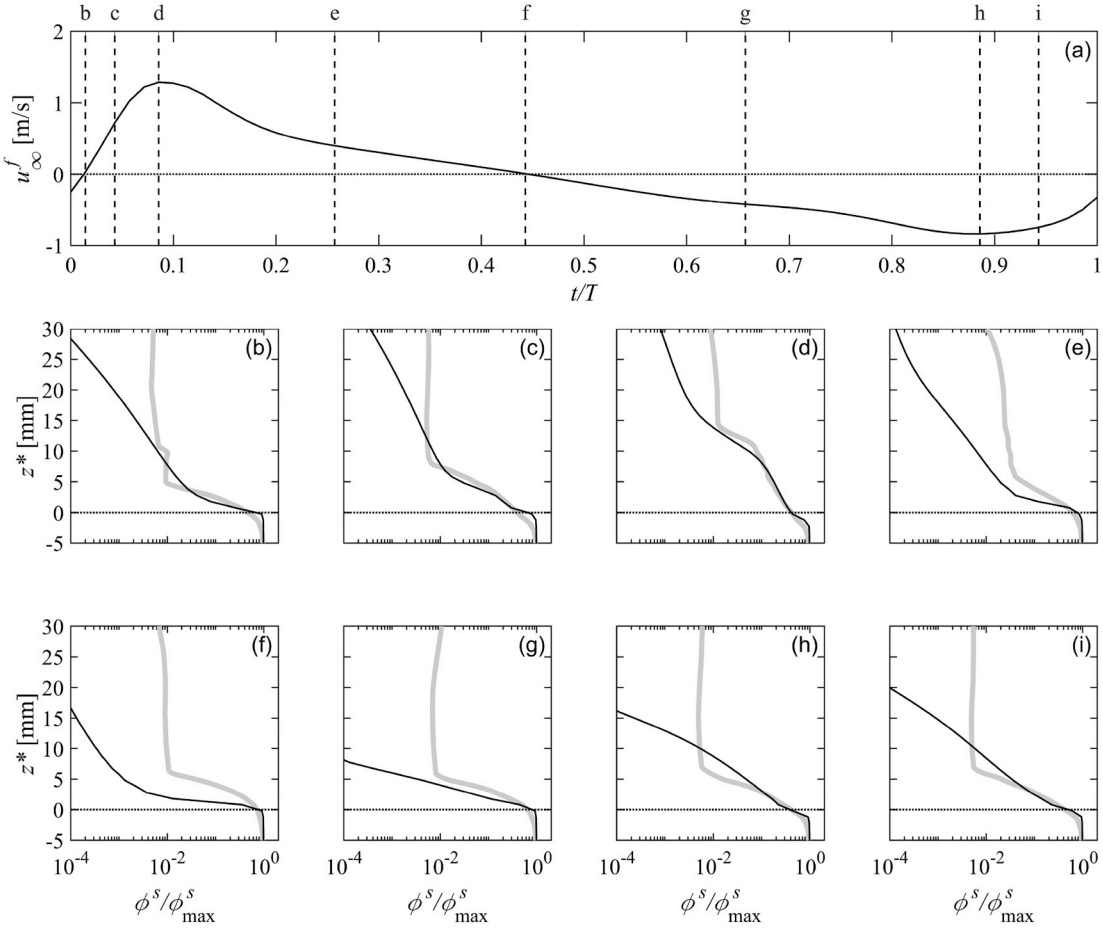

Fig. 8. (a) Time series of modeled u^f_∞ at $x = 0$. (b) – (i) are measured (gray curves) and modeled (black curves) vertical profiles of ϕ^s/ϕ^s_{max} at (b) $t/T = 0.014$, (c) $t/T = 0.043$, (d) $t/T = 0.086$, (e) $t/T = 0.257$, (f) $t/T = 0.443$, (g) $t/T = 0.657$, (h) $t/T = 0.886$, (i) $t/T = 0.943$ on a semi-log scale.

$$u^s(t/T, z^*)_n = u^f(t/T, z^*_s)_n\left(\frac{z^* - z^*_{\text{bed}}}{\delta_s}\right)^{\alpha}_n \tag{14}$$

where n represents each wave (i.e., ensemble), and α is a profile shape parameter ($0 < \alpha \leq 1$) (Sumer et al., 1996; Pugh and Wilson, 1999; Wang and Yu, 2007; Puleo et al., 2017), where $\alpha = 1.0$ is a linear profile. It is important to point out that this formula assumes u^s at z^*_s to be equal to the measured velocity from the ADPV. The model results confirm that u^f and u^s are identical at the top of sheet flow layer ($z^* = z^*_s(t)$) where $IA = 1$ and NRMSE = 0.1% (Fig. 9a). Comparing the u^s profiles calculated by SedWaveFoam with those from Eq. (14), it was found that $\alpha = 1.0$ (i.e., a linear profile) gave the smallest NRMSE and largest IA (not shown here). Hence, $\alpha = 1.0$ is adopted to reproduce the full profile of streamwise velocity in the measured data. In addition, the results of using a square-root-shaped ($\alpha = 0.5$) profile to approximate the streamwise velocity in the sheet flow layer are also presented.

The time-dependent q^s was calculated by integrating the horizontal sediment flux over the water column as:

$$q^s(t/T) = \int_{z^*_{\text{bed}}(t)}^{z^*_1(t)} \phi^s(t/T, z^*)u^s(t/T, z^*)dz^* \tag{15}$$

where z_1 represents the vertical elevation where $\phi^s/\phi^s_{max} = 0.01$. It should be reiterated here that $\phi^s/\phi^s_{max} < 0.01$ were excluded for both measured and modeled q^s due to the wash load discussed before, and contribution of $\phi^s/\phi^s_{max} < 0.01$ to sediment transport rate was much smaller than that of $\phi^s/\phi^s_{max} \geq 0.01$ in the model results. SedWaveFoam results (modeled) are compared with estimated q^s (measured) for both $\alpha = 0.5$ and 1.0 (Fig. 9c). Measured q^s using $\alpha = 1.0$ agrees reasonably well with the SedWaveFoam results. However, measured q^s magnitude using $\alpha = 0.5$ (gray dashed curve in Fig. 9c) is larger compared to the other two curves, particularly under the wave crest. The IA and NRMSE of SedWaveFoam results compared with measured q^s were 0.968 (0.919) and 8.5% (16.1%) with reference to the α-fitted measured data using $\alpha = 1.0$ ($\alpha = 0.5$). Some discrepancies between model results and measured data may be attributed to the smoothed vertical profile of measured ϕ^s which was multiplied with u^s without any correction for potentially over- or under-predicted sediment concentrations during low-flow phases in the wave cycle (i.e., small sheet flow layer thickness) (see Figs. 7 and 8). However, the smoothing effect becomes negligible for increasing sheet flow layer thickness ($\gtrsim 6$ mm), when the magnitude of the time-dependent sediment transport rate is largest. Measured wave-averaged sediment transport rate (net sediment transport rate), $\langle q^s \rangle$, was 115.77 mm^2/s using $\alpha = 1.0$ and 148.86 mm^2/s using $\alpha = 0.5$. Hence, q^s in the sheet flow layer is sensitive to the approximation of the shape of the u^s profile in the sheet flow layer, as $\langle q^s \rangle$ varies by roughly 30% depending on the α value. Modeled $\langle q^s \rangle$ was 102.58 mm^2/s, which is within 11.4% discrepancy compared with the measured data using $\alpha = 1.0$.

4. Discussion

4.1. Effect of progressive wave streaming

Net onshore sediment transport can be enhanced under free surface waves due to the effect of progressive wave streaming (Nielsen, 2006; Holmedal and Myrhaug, 2009; Kranenburg et al., 2012, 2013; Fuhrman et al., 2013; Kim et al., 2018), a process not present in OWTs. Following the methodology used by Kim et al. (2018), the 1DV SedFoam model is

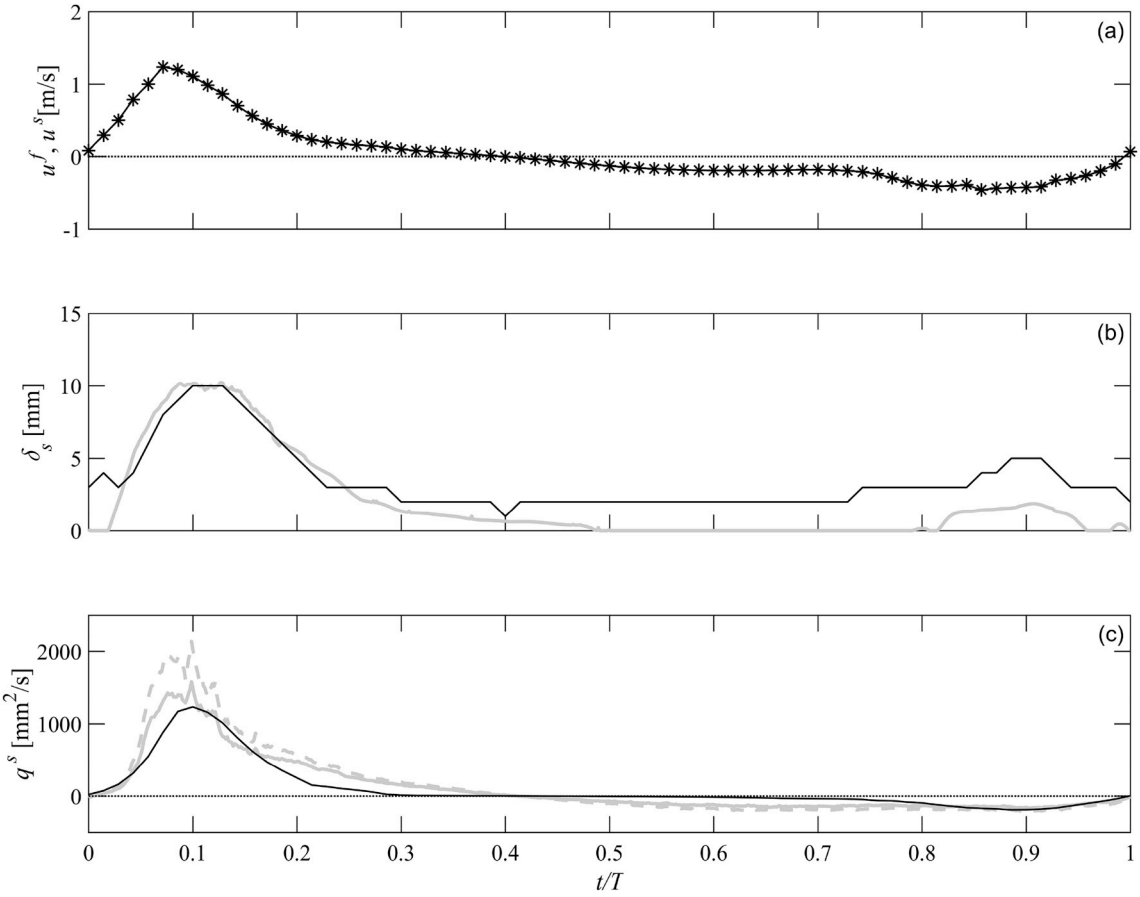

Fig. 9. Time series of (a) modeled u^f (solid curve) and u^s (asterisks) at $z^* = z_s(t)$ and $x = 0$. (b) δ_s of measured data (gray curve) and model results (black curve), and (c) q^s of measured data (gray solid curve, using u^s with $\alpha = 1.0$; gray dashed curve, using u^s with $\alpha = 0.5$) and model results (black solid curve).

applied to simulate the S1T7H60 case without a free surface to contrast the results with SedWaveFoam so that free surface effects can be isolated. It should be noted here that the main differences between SedWaveFoam and 1DV SedFoam are that SedWaveFoam results include the progressive wave streaming effect (Nielsen, 2006; Holmedal and Myrhaug, 2009; Kranenburg et al., 2012, 2013; Fuhrman et al., 2013; Kim et al., 2018) and converging-diverging effect on a sloping bed (Sumer et al., 1993; Fuhrman et al., 2013). A simple scaling analysis following Fuhrman et al. (2013) suggests that for the present wave condition and beach slope, the converging-diverging effect may be of minor importance relative to the progressive wave streaming effect. Nevertheless, it is worthwhile to point out the possible effect of converging-diverging on a sloping beach when interpreting the present model results. The vertical grid size and model parameters of 1DV SedFoam are identical to those used in the validated SedWaveFoam model. Flow is driven in the SedFoam model by a prescribed horizontal pressure gradient (f_{ext}) calculated using the streamwise flow velocity (u^f) of SedWaveFoam at $z^* = 0.15$ m (sufficiently far enough from the WBBL) with $f_{ext} = -\partial p^f/\partial x = \rho^f \partial u^f/\partial t$ following the boundary layer approximation. Consistent with previous analysis, SedFoam model results under the seventh wave are selected for the model inter-comparison.

The time series of u^f at $z^* = 0.1$ m produced by the 1DV SedFoam simulation is almost identical to that of SedWaveFoam ($IA > 0.999$ and NRMSE = 1.4% in Fig. 10a). Thus, the external forcing condition imposed to the 1DV SedFoam model is appropriate for a direct comparison of sheet flow dynamics between the models. The time-dependent WBBL thickness is estimated as $\delta_w = z_w^* - z_{bed}^*$ where z_w represents the velocity profile overshoot, defined as the vertical elevation of maximum u^f in time (Jensen et al., 1989; O'Donoghue and Wright, 2004b; Kim et al., 2018). The overshoot of u^f is less easily discernible during the wave trough under free surface waves, leading to the inability to determine z_w^* for SedWaveFoam results occasionally. In general, the increase of δ_w is more rapid when a free surface is included (SedWaveFoam), but maximum δ_w values from both models are similar (Fig. 10b) with a maximum WBBL thickness of about 30 mm.

Both models illustrate large TKE under the wave crest (k^f_{max} of 0.021 m^2/s^2 in SedWaveFoam and k^f_{max} of 0.017 m^2/s^2 in 1DV SedFoam) compared to that under the wave trough (k^f_{max} of 0.007 m^2/s^2 in SedWaveFoam and k^f_{max} of 0.006 m^2/s^2 in 1DV SedFoam) due to velocity skewness (Fig. 10f–g). This feature is known to cause turbulence asymmetry which leads to wave shape streaming (Kranenburg et al., 2012) and an offshore-directed mean current. Both models show consistent offshore-directed wave-averaged streamwise fluid velocity, $\langle u^f \rangle$, approaching -0.14 m/s, sufficiently away from the sediment bed ($z^* > 0.1$ m, Fig. 10e). Near the sediment bed, however, the vertical profile of u^f in SedWaveFoam is more onshore-directed, particularly under the wave crest (Fig. 10c) owing to the onshore-directed progressive wave streaming. Here, the progressive wave streaming-induced mean current is computed through the wave-averaged instantaneous velocity difference between the two models (i.e., $\langle u^f_{diff} \rangle = \langle u^f_{SedWaveFoam} - u^f_{SedFoam} \rangle$). The vertical profile of $\langle u^f_{diff} \rangle$ shows onshore-directed current with a peak velocity ($\langle u^f_{diff} \rangle_{max}$) of 0.056 m/s at $z^* = 0.017$m (Fig. 10e) which is inside the WBBL. Notice that the mean current of SedWaveFoam mostly remains to be offshore-directed due to the stronger effect from the wave shape streaming, but it is evident that the progressive wave streaming causes the magnitude of the offshore-directed mean flow to be reduced within the WBBL. When a free surface is included, two different boundary layer streaming mechanisms generate competing currents which induce stronger shear in

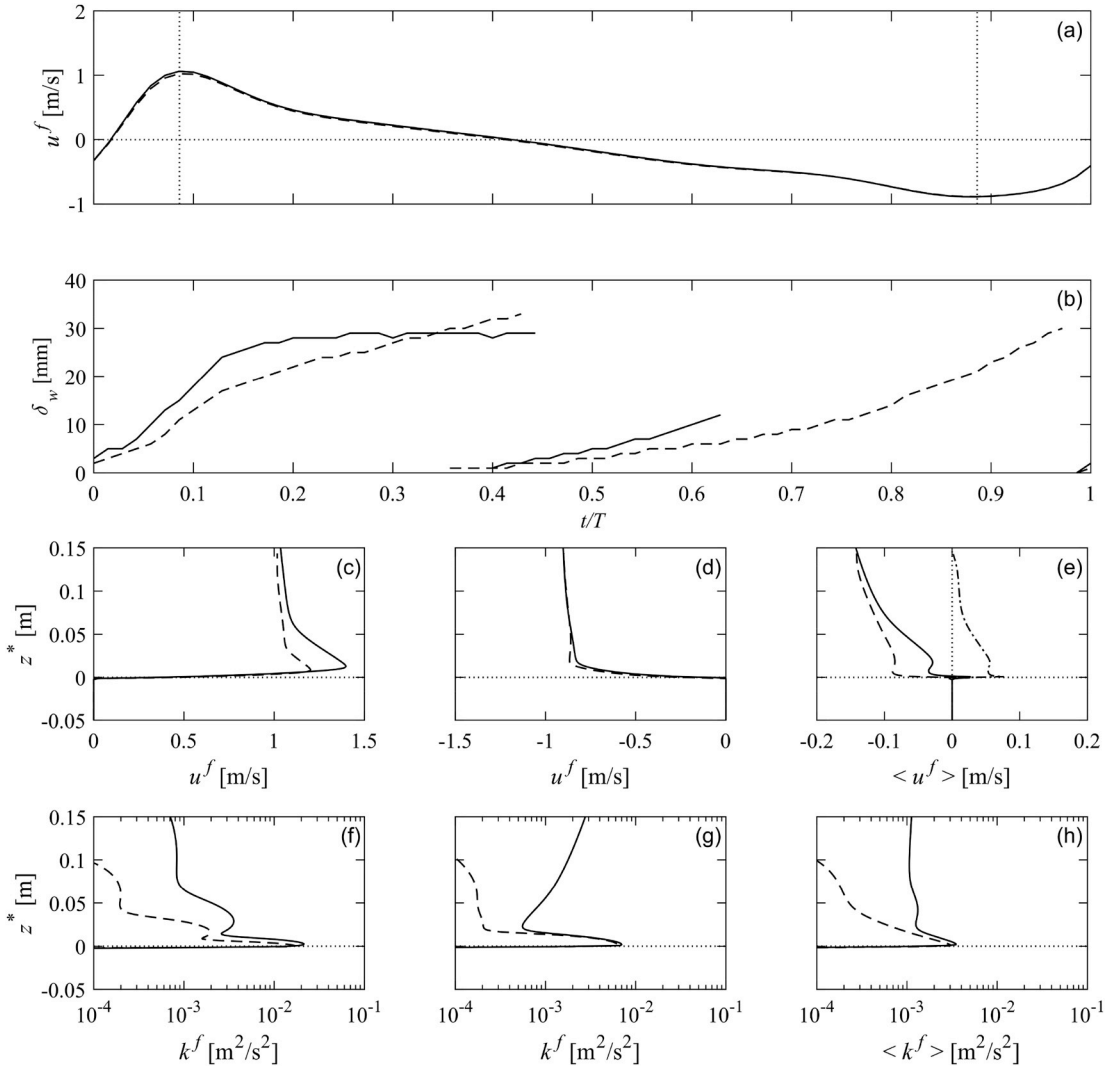

Fig. 10. Model comparisons of fluid phase characteristics (SedWaveFoam: solid curves; 1DV SedFoam: dashed curves). (a) Time series of u^f at $z^* = 0.1$ m and (b) wave boundary layer thickness. (c) and (f) are vertical profiles of u^f and k^f under the wave crest (t/T= 0.086), and (d) and (g) under the wave trough (t/T= 0.886). (e) and (h) are wave-averaged vertical profiles of u^f and k^f, respectively. The dash-dotted curve in (e) represents $\langle u^f_{\text{diff}} \rangle$.

flows, resulting in one order of magnitude larger TKE (Fig. 10f–h) above the WBBL ($z^* > 30$ mm). The progressive wave streaming-induced mean current for near-breaking waves is about 30% larger than that observed under nonbreaking waves where $\langle u^f_{\text{diff}} \rangle_{\max}$ was computed as 0.044 m/s in Kim et al. (2018); although, $u^f_{\text{RMS}} = \sqrt{\langle (u^f - \langle u^f \rangle)^2 \rangle}$ (computed at 0.15 m above the sediment bed for both results) is smaller for BARSED ($u^f_{\text{RMS}} = 0.31$ m/s) compared to that under nonbreaking waves ($u^f_{\text{RMS}} = 0.64$ m/s). The difference suggests there is an additional mechanism altering (enhancing) the streaming current. As will be discussed later, larger magnitude horizontal pressure gradient (characterized by $\dot{u}^f_\infty$) for near-breaking waves can be considered a major factor enhancing the streaming current.

To study sheet flow processes in detail, the vertical profiles of ϕ^s (top row), u^s (middle row), and streamwise sediment fluxes, $\phi^s u^s$, (bottom row) under the wave crest (left column), wave trough (middle column) and the corresponding wave-averaged profiles (right column) are shown in Fig. 11. Under the wave crest, sediment was suspended higher in the water column (Fig. 11a) with larger magnitude in u^s in the onshore direction (Fig. 11d) when a free surface was included (SedWaveFoam), and the resulting wave-averaged onshore sediment flux, $\langle \phi^s u^s \rangle$, was significantly larger than for the OWT-driven (1DV SedFoam) results (Fig. 11i). On the contrary, the corresponding vertical profiles of ϕ^s, u^s, and $\phi^s u^s$ were similar under the wave trough (Fig. 11b, e, h) for both model simulations. The free surface enhances net onshore flux (Fig. 11i) with the major difference occurring within the WBBL. The increase of onshore-directed $\phi^s u^s$ due to the free surface effect was previously shown to be 59% for nonbreaking velocity-skewed waves for $d_{50} = 0.24$ mm and wave velocity skewness of 0.39 (see Table 1 for more information) (Kim et al., 2018), compared with identical forcing with no free surface. The enhancement in net sediment transport rate was explained by a wave-stirring mechanism in which greater sediment concentration associated with a velocity-skewed wave crest was carried onshore by the progressive wave streaming-induced current. For the present near-breaking waves with both large velocity and acceleration skewness, the wave-averaged net onshore sediment transport rate was increased by 346% due to the free surface effect (see Table 1), nearly 6 times the effect for the nonbreaking velocity-skewed condition reported by Kim et al. (2018). The more significant enhancement of onshore sediment transport for the near-breaking wave condition must be further related to additional mechanisms that serve to enhance the wave-stirring effect (see Section 4.2).

Further insights into sediment transport are found by separating the sediment flux into current- and wave-induced components. For the Reynolds-averaged model results, the total wave-averaged sediment flux, $\langle \phi^s u^s \rangle$, was decomposed into the current-induced sediment flux, $\langle \phi^s \rangle \langle u^s \rangle$, and wave-induced sediment flux, $\langle \tilde{\phi}^s \tilde{u}^s \rangle$ where

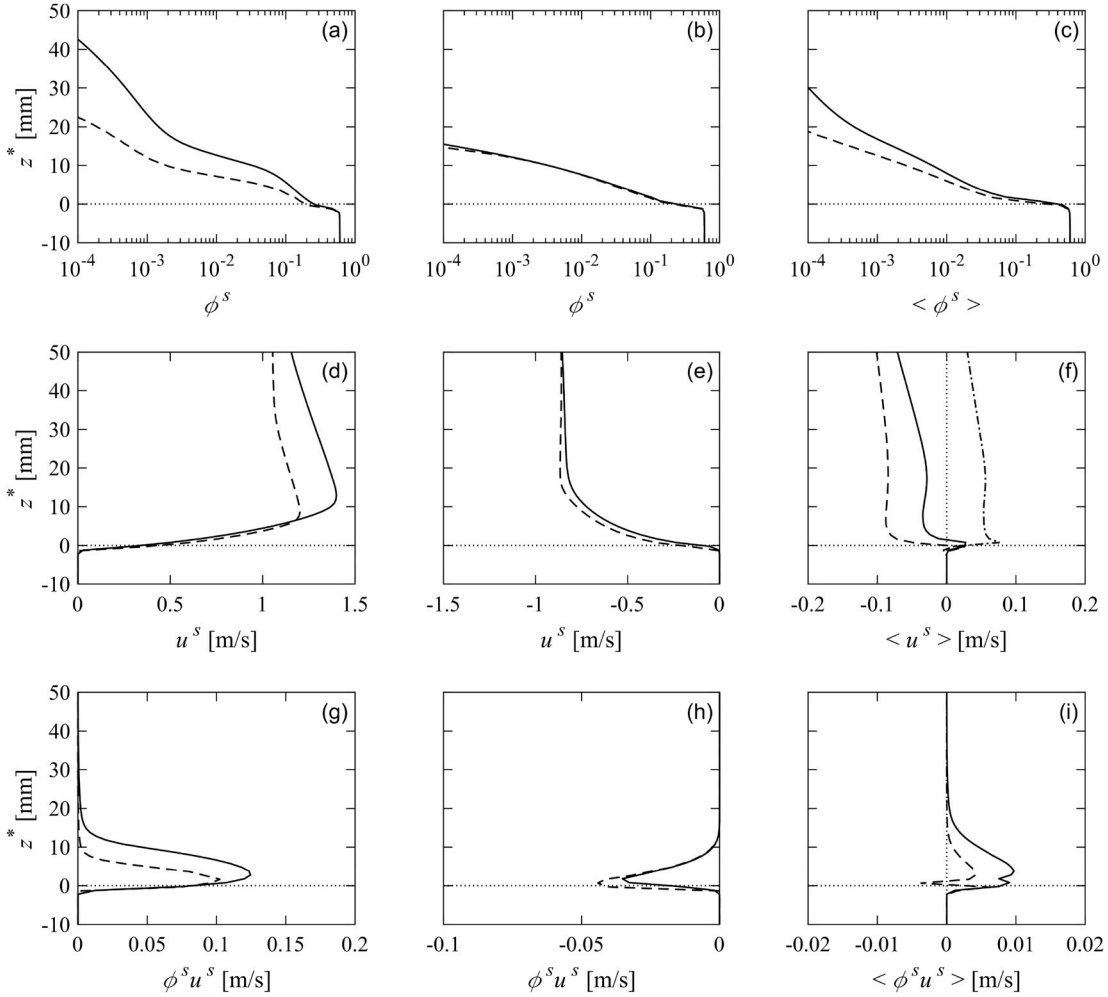

Fig. 11. Model comparisons of sediment phase characteristics (SedWaveFoam: solid curves; 1DV SedFoam: dashed curves). (a), (d), and (g) are vertical profiles of ϕ^s, u^s, and $\phi^s u^s$ under the wave crest (t/T= 0.086), and (b), (e), and (h) under the wave trough (t/T= 0.886). (c), (f), and (i) are wave-averaged vertical profiles of ϕ^s, u^s, and $\phi^s u^s$, respectively. The dash-dotted curve in (f) represent $\langle u^s_{\text{diff}} \rangle$.

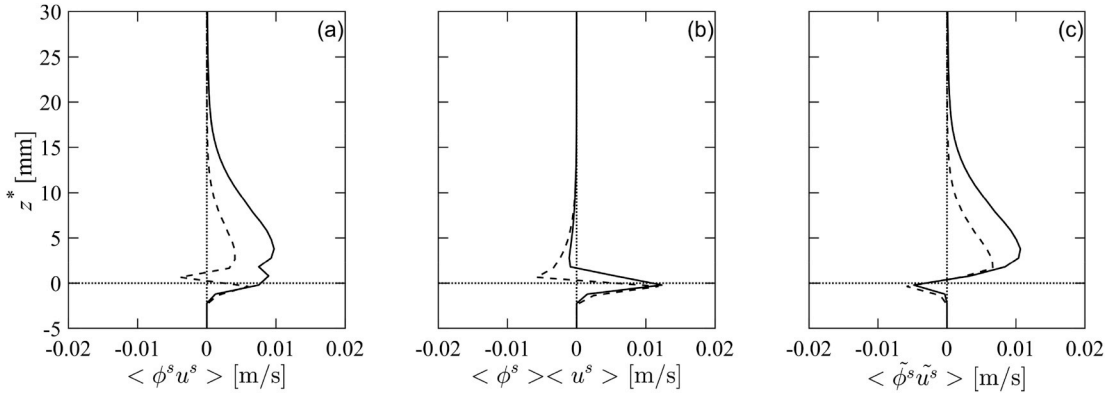

Fig. 12. Contributions to (a) $\langle \phi^s u^s \rangle$ from (b) $\langle \phi^s \rangle \langle u^s \rangle$ and (c) $\langle \tilde{\phi}^s \tilde{u}^s \rangle$ of SedWaveFoam (solid curves) and 1DV SedFoam (dashed curves).

$\phi^s(t/T, z^*) = \langle \phi^s(z^*) \rangle + \tilde{\phi}^s(t/T, z^*)$ and $u^s(t/T, z^*) = \langle u^s(z^*) \rangle + \tilde{u}^s(t/T, z^*)$ (Fig. 12). Below $z^* = 0$, the results from SedWaveFoam and 1DV SedFoam were similar, showing onshore flux in $\langle \phi^s \rangle \langle u^s \rangle$ and offshore flux in $\langle \tilde{\phi}^s \tilde{u}^s \rangle$ profiles. Both models indicate that the resulting total flux $\langle \phi^s u^s \rangle$ below $z^* = 0$ was onshore-directed. Above $z^* \sim 2$ mm, all fluxes (total, wave, and current) from SedWaveFoam were onshore-directed, markedly different from the 1DV SedFoam flux profiles. The increase in magnitude of $\langle \phi^s u^s \rangle$ from SedWaveFoam is attributed to the progressive wave streaming, particularly from $\langle \tilde{\phi}^s \tilde{u}^s \rangle$. In other words, a small mean current (see Fig. 11f) induces a considerable net onshore sediment transport when there is substantial sediment suspension under the wave crest (see Fig. 11a). This observation is consistent with the wave-stirring effect identified by Kim et al. (2018) for nonbreaking waves. However, the net onshore sediment flux is much more enhanced for near-breaking waves (Fig. 12a) compared to that for nonbreaking waves (see Fig. 9 in Kim et al., 2018), despite similar flow intensities in terms of velocity skewness (R and Sk_u; Table 1). The role of the horizontal pressure gradient associated with high acceleration skewness

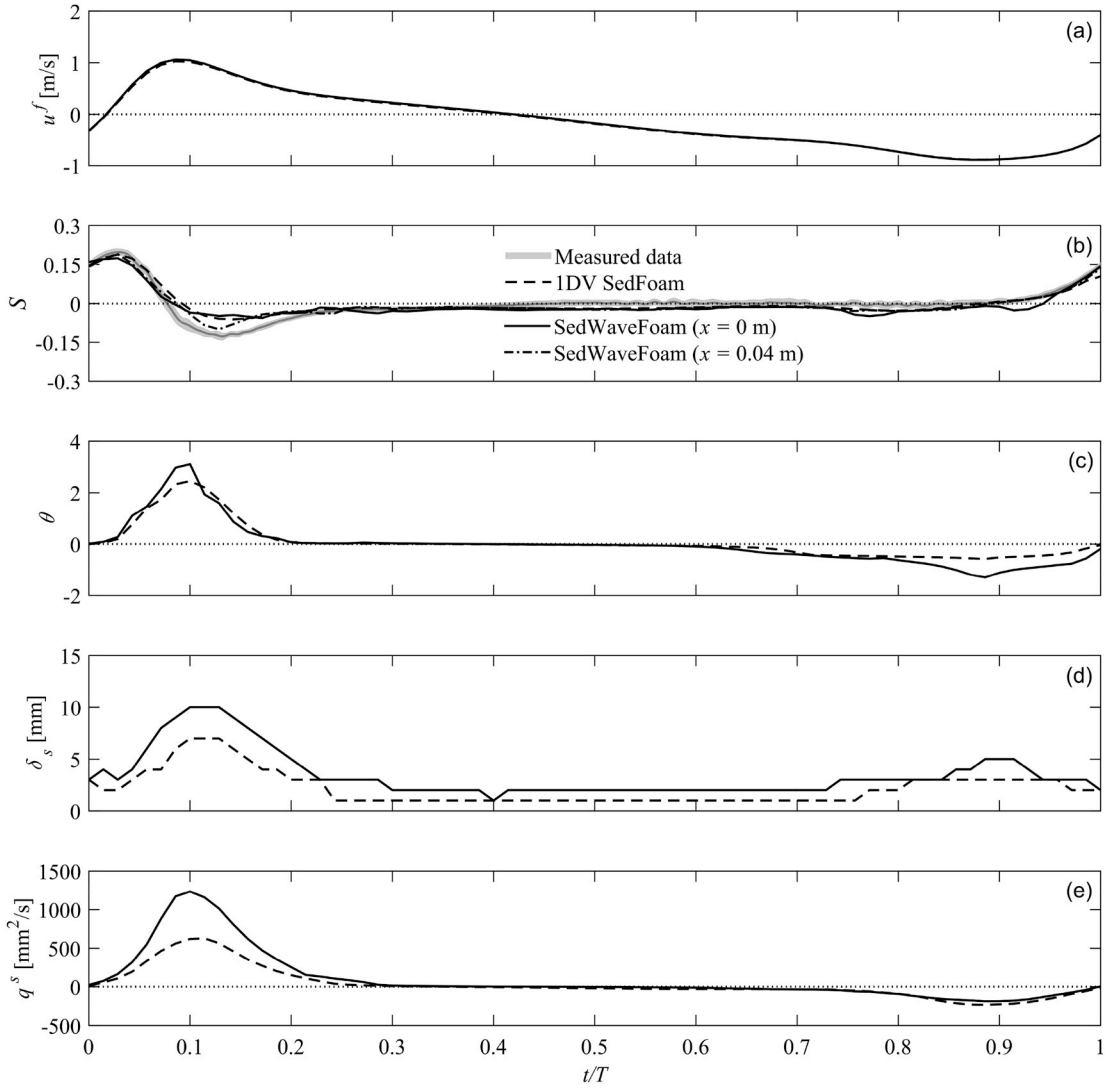

Fig. 13. Time series of (a) modeled (SedWaveFoam at $x = 0$: black solid curves; 1DV SedFoam: black dashed curves) u^f at $z^* = 0.10$ m, (b) measured (gray curve, phase-averaged; gray envelope, ± 1 standard deviation) and modeled S at $z^* = -7.3$ mm (black solid curve), (c) modeled θ, (d) modeled δ_s, and (e) modeled q^s. The black dash-dotted curve in panel (b) represents S from SedWaveFoam at $x = 0.04$ m and $z^* = -7.3$ mm.

(characterized by β and Sk_a), a feature unique to the present near-breaking wave conditions from BARSED, is illustrated in the next section.

4.2. Effect of horizontal pressure gradient

Non-dimensionalized horizontal pressure gradient, i.e., Sleath parameter, S, is calculated as

$$S = -\frac{\partial p^f/\partial x}{(\rho^s - \rho^f)g}. \tag{16}$$

The time series of S for SedWaveFoam and 1DV SedFoam model results are compared with the measured data (Fig. 13b). For reference, the time series of u^f is also presented (Fig. 13a). In the measured data (Anderson et al., 2017), a third-order-accurate finite difference formula (Hoffman and Frankel, 2001; Suzuki et al., 2010) was employed to calculate the horizontal pore pressure gradient (over a horizontal span of 0.08 m in the cross-shore), where the vertical elevation of the pressure transducers was 5~10 mm below the initial sediment bed level. For the SedWaveFoam model, the horizontal pore pressure gradient was calculated at $z^* = -7.3$ mm using a central difference method (over a horizontal span of 0.004 m in the cross-shore). The spatial variability resolved by the SedWaveFoam model is shown via two time series of S at different cross-shore locations, $x = 0$ and 0.04 m (Fig. 13b). Following the boundary layer approximation, the horizontal pore pressure gradient of 1DV SedFoam is $-\partial p^f/\partial x = \rho^f \partial u^f/\partial t$ and must be vertically uniform. Compared with the measured data, a notable discrepancy was observed in 1DV SedFoam results shortly after the flow peak ($0.1 < t/T < 0.2$) where $|S_{max}|$ was under predicted by roughly 50% in comparison with the measured data (black dashed curve versus gray curve in Fig. 13b). On the other hand, the SedWaveFoam model was able to predict the negative peak in S around $0.1 < t/T < 0.2$ at $x = 0.04$ m agreeing well with measured data ($IA = 0.966$ and NRMSE = 16.8%, black dash-dotted curve in Fig. 13b). Interestingly, an underestimation of the negative peak in S around $0.1 < t/T < 0.2$ also occurs at $x = 0$ for SedWaveFoam (black solid curve in Fig. 13b), more consistent with the 1DV SedFoam results. To summarize, the peak of horizontal pore pressure gradient in the surface layer of the sediment bed under wave crest observed in the measured data cannot be captured by 1DV model. More importantly, the SedWaveFoam model results indicate that the horizontal pore pressure gradient was not homogeneous in the streamwise direction. Within a spatial variability of only 0.04 m, the SedWaveFoam model showed a significant difference regarding the S peak shortly after the peak wave crest. It appears that under surface

waves with large acceleration skewness, large spatial variabilities in the sheet flow layer can exist. This spatial feature cannot be captured by the 1DV SedFoam model which assumes a homogeneous solution in the streamwise direction. The source of the spatial variability will be illustrated more clearly using the SedWaveFoam results later.

Non-dimensionalized bed shear stress is characterized via the Shields parameter, θ, as (Shields, 1936)

$$\theta = -\frac{\tau_b}{(\rho^s - \rho^f)gd_{50}}, \tag{17}$$

where the total bed shear stress, τ_b, is calculated as the sum of the fluid shear stress (τ^f) and particle shear stress (τ^s) at $z^* = 0$. The temporal evolution of θ, δ_s, and q^s between SedWaveFoam and 1DV SedFoam model results are given to further demonstrate the effect of a free surface (Fig. 13c–e). Berni et al. (2017) found that strong horizontal pressure gradients destabilize the sediment bed which may reduce the bed shear stress. SedWaveFoam model results presented here are consistent with this observation. Before the flow peak ($0 < t/T < 0.1$), the negative horizontal pore pressure gradient (or positive S) of $|S_{\max}| = 0.18$ acts in the opposite direction of the flow, stabilizing the sediment bed which increases the onshore-directed bed shear stress of SedWaveFoam. On the other hand, the more rapid decrease of θ after the flow peak ($0.1 < t/T < 0.2$) in the SedWaveFoam results is correlated with an increase of positive horizontal pore pressure gradient (or negative S) (Fig. 13b and c).

1DV SedFoam predicts smaller δ_s and q^s under the wave crest while the difference is less apparent at the wave trough (Fig. 13d and e). Maximum δ_s from SedWaveFoam was enhanced by 41.3% compared to that of 1DV SedFoam. For the present near-breaking waves, modeled q^s under the wave crest from SedWaveFoam was 1234.51 mm^2/s, which is 96.8% greater than $q^s_{\max}$ from 1DV SedFoam (627.33 mm^2/s). Under the wave trough, the difference between SedWaveFoam and 1DV SedFoam in q^s is relatively minor (Fig. 13e). The wave-averaged (i.e., net) sediment transport rate predicted by SedWaveFoam ($\langle q^s \rangle = 102.58$ mm^2/s) was 3.46 times larger than that of 1DV SedFoam ($\langle q^s \rangle = 29.63$ mm^2/s; see Table 1). Kim et al. (2018) showed that under nonbreaking waves, the enhanced onshore sediment transport particularly apparent under the wave crest with the presence of a free surface is associated with the wave-stirring effect combined with the progressive wave streaming. With similar flow intensity and velocity skewness (Table 1), the free surface effect on enhancing wave-averaged onshore sediment transport $\langle q^s \rangle$ for nonbreaking waves reported by Kim et al. (2018) was only 60%. Cheng et al. (2017) suggested that momentary bed failure may occur under combined high values of θ and S that further leads to instabilities within the sheet flow layer, which cannot be resolved by a 1DV model due to streamwise uniformity. When momentary bed failure occurs, the thickness of the mobilized sediment bed layer is significantly increased, often related to suddenly enhanced sediment transport via plug flow (Sleath, 1999; Foster et al., 2006). It is likely that momentary bed failure associated with large horizontal pressure gradients (i.e., large acceleration skewness) is occurring under the present near-breaking wave conditions, acting as an additional mechanism to enhance net onshore sediment transport in conjunction with the progressive wave streaming. It is important to point out that although there was large spatial variability in S in the streamwise direction, the corresponding spatial variabilities of δ_s and q^s were minor (at $x = 0.04$ m, NRMSEs are 3.9% and 1.6% for δ_s and q^s, respectively, compared to those at $x = 0$).

The spatial variability of S and fluid vorticity ($\omega^f = du^f/dz - dw^f/dx$) are investigated using SedWaveFoam results to shed more light on possible momentary bed failure (Fig. 14). The spatial variability in S is associated with near-bed vorticity. Under the wave crest (Fig. 14a and c), three locations of large $|S|$ approaching 0.2 were observed. These locations also coincide with high fluid vorticity ω^f near the sediment bed. These vorticity "hot spots" are present under the wave crest with high flow acceleration (Fig. 14a and c), but almost disappear under the wave trough (Fig. 14b and d). The spatial variation of S (or ω^f) shown in Fig. 14a (Fig. 14b) explains why SedWaveFoam pressure gradient results at $x = 0$ differed significantly from those at $x = 0.04$ m, under the wave crest (Fig. 13b), as the "hot spots" were sparsely distributed with a local length scale of about 2 cm, coincident with the bed level change. It should also be noted that the bed level change is not always associated with large fluctuations of S nor ω^f under the wave trough (Fig. 14c and d), in which large S and θ are essential to trigger the momentary bed failure. Overall, the intermittent spatial fluctuation of S under the wave crest is consistent with the concept of momentary bed failure. 2DV SedFoam was also utilized to double-check the generation of near-bed instabilities. Qualitatively similar spatial fluctuations of S and ω^f existed in the 2DV SedFoam results (not shown here). Thus, a two-dimensional model is essential to resolve the effect of momentary bed failures, which is necessary to reproduce observed enhanced net onshore sediment transport.

To further understand why net onshore sediment transport due to the free surface effect under nonbreaking waves reported by Kim et al. (2018) is much smaller than the present near-breaking case (BARSED), the spatial evolutions of S, ω^f, and ϕ^s of these two cases under the wave crest ($t/T = 0.114$ for BARSED and $t/T = 0.205$ for nonbreaking wave) are presented in Fig. 15. Although the setups and dimensionless parameters between the two cases vary (e.g., wave condition, water depth, and sheet flow layer thickness), this analysis has qualitative and comparative value since it was evident that momentary bed failure enhancing onshore sediment transport did not occur in the case studied in Kim et al. (2018). The present BARSED case has about 2.5 times larger $|S_{\max}|$ than that in Kim et al. (2018), due to greater β and Sk_a (Table 1). As expected, the spatial fluctuation of S and ω^f are substantial in BARSED, and hence sediment concentration ϕ^s also shows significant variation in the streamwise direction. In contrast, the nonbreaking wave case showed much less spatial fluctuations in these quantities.

The combined effects of large horizontal pressure gradients associated with high acceleration skewness and large bed shear stress likely trigger near-bed instabilities, and drive more sediment suspension (Fig. 11a) and onshore directed current (see $\langle u^f_{\text{diff}} \rangle_{\max}$ in Table 1). Hence, the net onshore wave-induced sediment flux ($\langle \tilde{\phi}^s \tilde{u}^s \rangle$) (Fig. 12c), and sediment transport rate (q^s) are significantly increased. In other words, through numerical experiments with and without the presence of a free surface and comparison with earlier model results without large acceleration skewness, it was demonstrated that nonlinear interactions between acceleration skewness, velocity skewness, and progressive wave streaming can significantly enhance net onshore sediment transport.

5. Conclusions

A numerical investigation of sheet flow under near-breaking surface waves was conducted using a free surface resolving Eulerian two-phase model, SedWaveFoam. The notable advantage of SedWaveFoam is that the flow fields under progressive waves over a complex bathymetry and resulting sediment transport processes can be concurrently resolved. In the present study, SedWaveFoam is fully validated with measured data (Anderson et al., 2017; Mieras et al., 2017, 2019). For the fluid characteristics, SedWaveFoam yielded excellent agreement with measured free surface elevation, streamwise and vertical velocities. For the WBBL and sediment transport characteristics, the vertical profiles of streamwise velocity, TKE, volumetric sediment concentration, and sheet flow layer thickness show good agreement with measured data. Sediment transport rates using the α-fitting method are comparable with SedWaveFoam results.

The 1DV SedFoam simulation representing conditions without a free surface is also carried out and the results are compared with SedWaveFoam model results to identify the different sediment transport mechanisms driving onshore sediment transport. Consistent with the sediment transport under nonbreaking waves (Kim et al., 2018), the near-bed flow velocity and sediment flux are more onshore-directed by

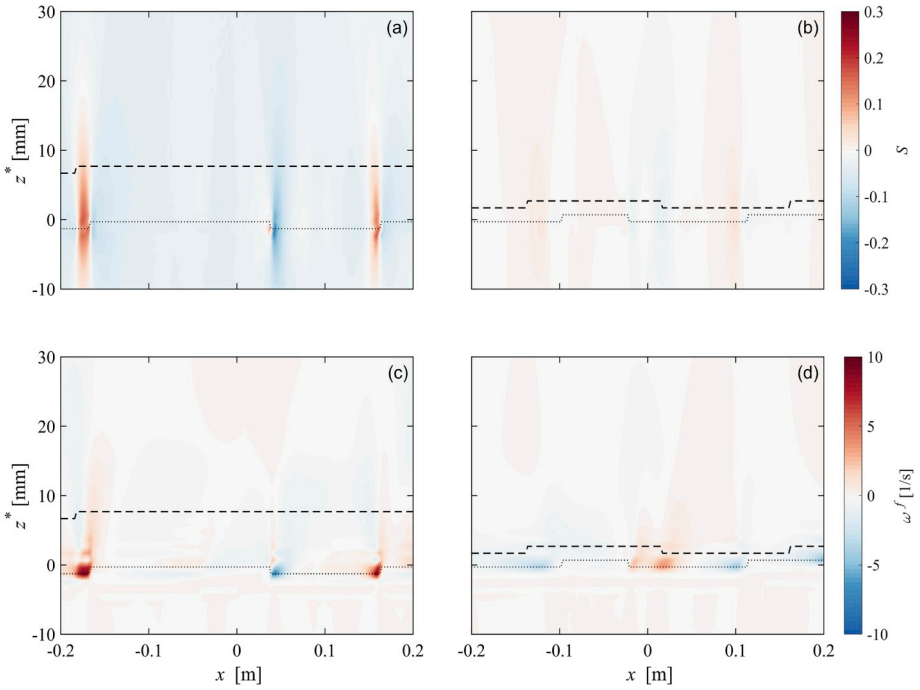

Fig. 14. The $x - z^*$ snapshots of (a–b) S and (c–d) ω^f, under (a, c) the wave crest ($t/T = 0.114$) and (b, d) the wave trough ($t/T = 0.886$). The black dashed and black dash-dotted curves represent z_s^* and z_{bed}^*, and t/T values are with reference to $x = 0$.

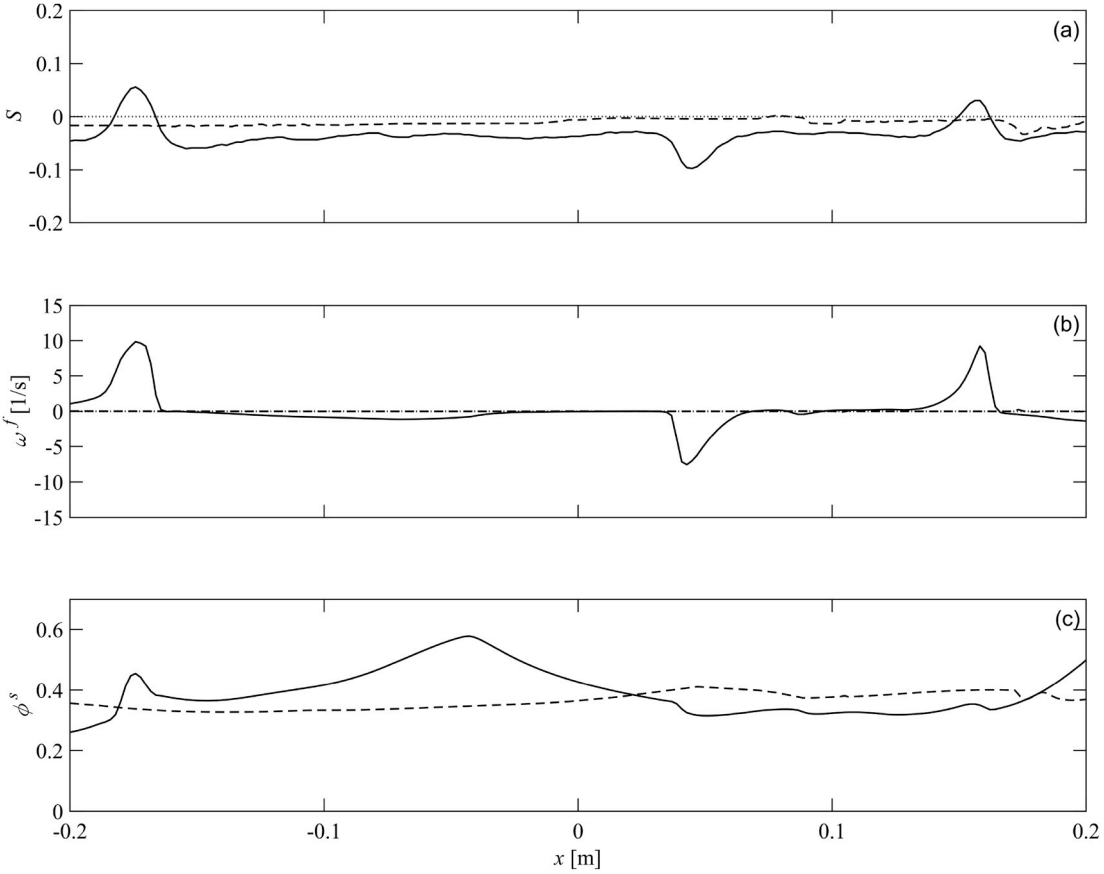

Fig. 15. Comparisons between the present near-breaking wave case from BARSED (solid curves) and a nonbreaking wave case in Kim et al. (2018) (dashed curves) (see Table 1). The spatial evolution of (a) S at $z^* = -7.3$ mm, (b) ω^f at $z^* = -1$ mm, and (c) ϕ^s at $z^* = -1$ mm under the wave crest ($t/T = 0.114$ for BARSED, and $t/T = 0.205$ for nonbreaking wave).

including the free surface; consistent with the effect of progressive wave streaming. However, it is evident that for the near-breaking waves, onshore sediment transport is further enhanced due to a large horizontal pressure gradient. Model results indicate that the combined effect of large horizontal pressure gradient and bed shear stress triggers near-bed instability of the sheet flow layer where the instantaneous near-bed vortices are generated enhancing sediment transport under the wave crest. The locations where near-bed instabilities take place coincide with the occurrence of large horizontal pore pressure gradient in the time series during the wave crest consistent with measured data. The joint effects of progressive wave streaming and near-bed instability drive increased sediment suspension and enhanced onshore sediment transport, which are much greater than those only with the progressive wave streaming effect in nonbreaking waves (Kim et al., 2018). The analyses presented in this study were based on a single sediment size of d_{50} = 0.17 mm. It is expected that the interplay between the free surface effect, velocity skewness, and acceleration skewness may be altered for different sediment sizes. For a comprehensive understanding, a variety of sediment sizes and wave conditions should be investigated.

Acknowledgments

This study is supported by NSF (OCE-1635151; OCE-1356855; OCE-1356978) and Office of Naval Research (N00014-18-1-2785). Numerical simulations presented in this study were carried out using the Mills cluster at University of Delaware, and the SuperMic cluster at Louisiana State University via XSEDE (TG-OCE100015). Z. Cheng would like to thank the support of postdoctoral scholarship from Woods Hole Oceanographic Institution. We are grateful to the developers involved in OpenFOAM who are the foundation of the model presented in this paper. We would also like to thank the two anonymous reviewers for their comments and insights into the cause of fictitious TKE generation in the near potential-flow region of a wave field. The source code of SedWaveFoam and the case setup to reproduce the same results is publicly available via Community Surface Dynamics Modeling System (CSDMS) model repository maintained by GitHub: https://github.com/sedwavefoam/sedwavefoam (source code) and https://github.com/sedwavefoam/BARSED (case setup). BARSED data used in this manuscript were obtained through DesignSafe-CI (https://doi.org/10.17603/DS2768V).

References

Aagaard, T., Hughes, M.G., 2010. Breaker turbulence and sediment suspension in the surf zone. Mar. Geol. 271, 250–259. https://doi.org/10.1016/j.margeo.2010.02.019.

Aagaard, T., Black, K.P., Greenwood, B., 2002. Cross-shore suspended sediment transport in the surf zone: a field-based parameterization. Mar. Geol. 185, 283–302.

Anderson, D., Cox, D., Mieras, R., Puleo, J.A., Hsu, T.-J., 2017. Observations of wave-induced pore pressure gradients and bed level response on a surf zone sandbar. J. Geophys. Res. Ocean. 122, 5169–5193. https://doi.org/10.1002/2016JC012557.

Austin, M., Masselink, G., O'Hare, T., Russel, P., 2009. Onshore sediment transport on a sandy beach under varied wave conditions: flow velocity skewness, wave asymmetry or bed ventilation? Mar. Geol. 259, 86–101. https://doi.org/10.1016/j.margeo.2009.01.001.

Berberović, E., van Hinsberg, N.P., Jakirlić, S., Roisman, I.V., Tropea, C., 2009. Drop impact onto a liquid layer of finite thickness: dynamics of the cavity evolution. Phys. Rev. E79, 036306. https://doi.org/10.1103/PhysRevE.79.036306.

Berni, C., Michallet, H., Barthélemy, E., 2017. Effects of horizontal pressure gradients on bed destabilization under waves. J. Fluid Mech. 812, 721–751. https://doi.org/10.1017/jfm.2016.805.

Brown, S.A., Greaves, D.M., Magar, V., Conley, D.C., 2016. Evaluation of turbulence closure models under spilling and plunging breakers in the surf zone. Coast. Eng. 114, 177–193. https://doi.org/10.1016/j.coastaleng.2016.04.002.

Chen, C.P., Wood, P.E., 1985. A turbulence closure model for dilute gas-particle flows. Can. J. Chem. Eng. 63 (3), 349–360. https://doi.org/10.1002/cjce.5450630301.

Cheng, Z., Hsu, T.–J., Calantoni, J., 2017. SedFoam: a multi-dimensional Eulerian two-phase model for sediment transport and its application to momentary bed failure. Coast. Eng. 119, 32–50. https://doi.org/10.1016/j.coastaleng.2016.08.007.

Danon, H., Wolfshtein, M., Hetsroni, G., 1977. Numerical calculations of two-phase turbulent round jet. Int. J. Multiph. Flow 3 (3), 223–234. https://doi.org/10.1016/0301-9322(77)90002-7.

Devolder, B., Rauwoens, P., Troch, P., 2017. Application of a buoyancy-modified k-ω SST turbulence model to simulate wave run-up around a monopile subjected to regular waves using OpenFOAM®. Coast. Eng. 125, 81–94. https://doi.org/10.1016/j.coastaleng.2017.04.004.

Ding, J., Gidaspow, D., 1990. A bubbling fluidization model using kinetic theory of granular flow. AIChE J. 36 (4), 523–538. https://doi.org/10.1002/aic.690360404.

Doering, J.C., Elfrink, B., Hanes, D.M., Ruessink, B.G., 2000. Parameterization of velocity skewness. In: Proc. 27th Conf. Coast. Eng., Sydney, Australia, pp. 1383–1396.

Dohmen-Janssen, C.M., Hanes, D.M., 2002. Sheet flow dynamics under monochromatic nonbreaking waves. J. Geophys. Res. 107 (C10). https://doi.org/10.1029/2001JC00104.

Dohmen-Janssen, C.M., Hassan, W.N., Ribberink, J.S., 2001. Mobile-bed effects in oscillatory sheet flow. J. Geophys. Res. Ocean. 106 (C11), 27103–27115. https://doi.org/10.1029/2000JC000513.

Dong, P., Zhang, K., 1999. Two-phase flow modelling of sediment motions in oscillatory sheet flow. Coast. Eng. 36 (2), 87–109.

Drake, T.G., Calantoni, J., 2001. Discrete particle model for sheet flow sediment transport in the nearshore. J. Geophys. Res. Ocean. 106 (C9), 19859–19868. https://doi.org/10.1029/2000JC000611.

Drew, D.A., 1983. Mathematical modeling of two-phase flow. Ann. Rev. Fluid Mech. 15. www.annualreviews.org/doi/pdf/10.1146/annurev.fl.15.010183.001401.

Fernández-Mora, A., Calvete, D., Falqués, A., de Swart, H.E., 2015. Onshore sandbar migration in the surf zone: new insights into the wave-induced sediment transport mechanisms. Geophys. Res. Lett. 42, 2869–2877. https://doi.org/10.1002/2014GL063004.

Foster, D.L., Bowen, A.J., Holman, R.A., Natoo, P., 2006. Field evidence of pressure gradient induced incipient motion. J. Geophys. Res. 106 (C9), 19859–19868.

Frank, D., Foster, D., Sou, I.M., Calantoni, J., 2015a. Incipient motion of surf zone sediments. J. Geophys. Res. Ocean. 120, 5710–5734. https://doi.org/10.1002/2014JC010424.

Frank, D., Foster, D., Sou, I.M., Calantoni, J., Chou, P., 2015b. Lagrangian measurements of incipient motion in oscillatory flows. J. Geophys. Res. Ocean. 120, 244–256. https://doi.org/10.1002/2014JC010183.

Fuhrman, D.R., Schløer, S., Sterner, J., 2013. RANS-based simulation of turbulent wave boundary layer and sheet-flow sediment transport processes. Coast. Eng. 73, 151–166. https://doi.org/10.1016/j.coastaleng.2012.11.001.

Gallagher, E.L., Elgar, S., Guza, R.T., 1998. Observations of sand bar evolution on a natural beach. J. Geophys. Res. 103, 3203–3215.

Garcez Faria, A.F., Thornton, E.B., Stanton, T.P., 1996. Small-scale morphology related to wave and current parameters over a barred beach. In: Proc. 25th Conf. Coast. Eng, Orlando, Florida, USA, pp. 3391–3404. https://doi.org/10.9753/icce.v25.%p.

Gidaspow, D., 1994. Multiphase Flow and Fluidization - Continuum and Kinetic Theory Descriptions. Academic, Pr.

Grasso, F., Castelle, B., B.G., Ruessink, 2012. Turbulence dissipation under breaking waves and bores in a natural surf zone. Cont. Shelf Res. 43, 133–141.

Henderson, S.M., Allen, J.S., Newberger, P.A., 2004. Nearshore sandbar migration predicted by an eddy-diffusive boundary layer model. J. Geophys. Res. 109 (C6), C06024. https://doi.org/10.1029/2003JC002137.

Hoffman, J.D., Frankel, S., 2001. Numerical Methods for Engineers and Scientists, second ed. CRC Press, New York.

Holmedal, L.E., Myrhaug, D., 2009. Wave-induced steady streaming, mass transport and net sediment transport in rough turbulent ocean bottom boundary layers. Cont. Shelf Res. 29 (7), 911–926. 2009. https://doi.org/10.1016/j.csr.2009.01.012.

Hsu, T.–J., Hanes, D.M., 2004. The effects of wave shape on sheet flow sediment transport. J. Geophys. Res. 109 (C5), C05025. https://doi.org/10.1029/2003JC002075.

Hsu, T.–J., Jenkins, J.T., Liu, P.L.-F., 2004. On two-phase sediment transport: sheet flow of massive particles. Proc. R. Soc. A Math. Phys. Eng. Sci. 460 (2048), 2223–2250. https://doi.org/10.1098/rspa.2003.1273.

Hsu, T.–J., Elgar, S., Guza, R., 2006. Wave-induced sediment transport and onshore sandbar migration. Coast Eng. 53 (10), 817–824.

Jackson, A., 2012. A comprehensive tour of snappyHexMesh. In: 7th OpenFOAM Workshop.

Jacobsen, N.G., Fuhrman, D.R., Fredsøe, J., 2012. A wave generation toolbox for the open-source CFD library: OpenFoam®. Int. J. Numer. Meth. Fluids 70 (9), 1073–1088. https://doi.org/10.1002/fld.2726.

Jenkins, J.T., Savage, S.B., 1983. A theory for the rapid flow of identical, smooth, nearly elastic, spherical particles. J. Fluid Mech. 130 (1), 187–202. https://doi.org/10.1017/S0022112083001044.

Jensen, B.L., Sumer, B.M., Fredsøe, J., 1989. Turbulent oscillatory boundary layers at high Reynolds numbers. J. Fluid Mech. 206 (1), 265–297. https://doi.org/10.1017/S0022112089002302.

Johnson, P.C., Jackson, R., 1987. Frictional-collisional constitutive relations for granular materials, with application to plane shearing. J. Fluid Mech. 176, 67–93.

Kim, Y., 2018. A Numerical Investigation of Turbulent Coherent Structures and Sediment Transport under Waves in Shallow Coastal Zone. PhD Thesis. Univ. of Delaware, Newark, DE, USA.

Kim, Y., Cheng, Z., Hsu, T.–J., Chauchat, J., 2018. A numerical study of sheet flow under monochromatic nonbreaking waves using a free surface resolving Eulerian two-phase flow model. J. Geophys. Res. Ocean. 123, 4693–4719. https://doi.org/10.1029/2018JC013930.

Klostermann, J., Schaake, K., Schwarze, R., 2012. Numerical simulation of a single rising bubble by VOF with surface compression. Int. J. Numer. Meth. Fluids 71 (8), 960–982. https://doi.org/10.1002/fld.3692.

Kranenburg, W.M., Ribberink, J.S., Uittenbogaard, R.E., Hulscher, S.J.M.H., 2012. Net currents in the wave bottom boundary layer: on waveshape streaming and progressive wave streaming. J. Geophys. Res.: Earth Surface. https://doi.org/10.1029/2011JF002070.

Kranenburg, W.M., Ribberink, J.S., Schretlen, J.J.L.M., Uittenbogaard, R.E., 2013. Sand transport beneath waves: the role of progressive wave streaming and other free surface effects. J. Geophys. Res. Earth Surface 118 (1), 122–139. https://doi.org/10.1029/2012JF002427.

Lanckriet, T., Puleo, J.A., Waite, N., 2013. A conductivity concentration profiler for sheet flow sediment transport. IEEE J. Ocean. Eng. 38 (1), 55–70. https://doi.org/10.1109/JOE.2012.2222791.

Lanckriet, T., Puleo, J., Masselink, G., Turner, I., Conley, D., Blenkinsopp, C., Russell, P., 2014. Comprehensive field study of swash-zone processes. II: sheet flow sediment concentrations during quasi-steady backwash. J. Waterw. Port, Coast. Ocean Eng. 140 (1), 29–42. https://doi.org/10.1061/(ASCE)WW.1943-5460.0000209.

Larsen, B.E., Fuhrman, D.R., 2018. On the over-production of turbulence beneath surface waves in Reynolds-averaged Navier-Stokes models. J. Fluid Mech. 853, 419–460. https://doi.org/10.1017/jfm.2018.577.

Li, M., Pan, S., O'Connor, B.A., 2008. A two-phase numerical model for sediment transport prediction under oscillatory sheet flows. Coast. Eng. 55 (12), 1159–1173.

Madsen, O.S., 1974. Stability of a sand bed under breaking waves. In: Proc. 14th Conf. Coast. Eng. pp. 776–794 (New York, USA).

Mieras, R.S., Puleo, J.A., Anderson, D., Cox, D.T., Hsu, T.–J., 2017. Large-scale experimental observations of sheet flow on a sandbar under skewed-asymmetric waves. J. Geophys. Res. Ocean. 122 (6), 5022–5045. https://doi.org/10.1002/2016JC012438.

Mieras, R.S., Puleo, J.A., Cox, D.T., Hsu, T.–J., 2018. Sandbar Sediment Transport, DesignSafe-CI. https://doi.org/10.17603/DS2768V.

Mieras, R.S., Puleo, J.A., Anderson, D., Hsu, T.–J., Cox, D.T., Calantoni, J., 2019. Relative contributions of bed load and suspended load to sediment transport under skewed-asymmetric waves on a sandbar crest. J. Geophys. Res. Ocean. 124, 1294–1321. https://doi.org/10.1029/2018JC014564.

Nielsen, P., 2006. Sheet flow sediment transport under waves with acceleration skewness and boundary layer streaming. Coast. Eng. 53 (9), 749–758. https://doi.org/10.1016/j.coastaleng.2006.03.006.

O'Donoghue, T., Wright, S., 2004a. Concentrations in oscillatory sheet flow for well sorted and graded sands. Coast. Eng. 50 (3), 117–138. https://doi.org/10.1016/j.coastaleng.2003.09.004.

O'Donoghue, T., Wright, S., 2004b. Flow tunnel measurements of velocities and sand flux in oscillatory sheet flow for well-sorted and graded sands. Coast. Eng. 51 (11–12), 1163–1184. https://doi.org/10.1016/j.coastaleng.2004.08.001.

Pugh, F.J., Wilson, K.C., 1999. Velocity and concentration distributions in sheet flow above plane beds. J. Hydr. Eng. 125 (2), 117–125. https://doi.org/10.1061/(ASCE)0733-9429(1999)125:2(117).

Puleo, J.A., Krafft, D., Pintado-Patiño, J.C., Bruder, B., 2017. Video-derived near bed and sheet flow sediment particle velocities in dam-break-driven swash. Coast Eng. 126, 27–36. https://doi.org/10.1016/j.coastaleng.2017.04.008.

Reniers, A.J.H.M., Thornton, E.B., Stanton, T.P., Roelvink, J.A., 2004. Vertical flow structure during sandy Duck: observations and modeling. Coast. Eng. 51, 237–260.

Ribberink, J.S., van der Werf, J.J., O'Donoghue, T., Hassan, W.N.M., 2008. Sand motion induced by oscillatory flows: sheet flow and vortex ripples. J. Turbul. 9, N20. https://doi.org/10.1080/14685240802220009.

Rodi, W., 1993. Turbulence Models and Their Application in Hydraulics. CRC Press.

Ruessink, B.G., Kuriyama, Y., 2008. Numerical predictability experiments of cross-shore sandbar migration. Geophys. Res. Lett. 35 (L01603).

Ruessink, B.G., Pape, L., Turner, I.L., 2009. Daily to interannual cross-shore sandbar migration: observations from a multiple sandbar system. Cont. Shelf Res. 29, 1663–1677.

Ruggiero, P., Kaminsky, G.M., Gelfenbaum, G., Voigt, B., 2005. Seasonal to interannual morphodynamics along a high-energy dissipative littoral cell. J. Coast. Res. 21 (3), 553–578.

Scott, C.P., Cox, D.T., Maddux, T.B., Long, J.W., 2005. Large-scale laboratory observations of turbulence on a fixed barred beach. Meas. Sci. Technol. 16 (10), 1903.

Scott, N.V., Hsu, T.-J., Cox, D., 2009. Steep wave, turbulence, and sediment concentration statistics beneath a breaking wave field and their implications for sediment transport. Cont. Shelf Res. 29, 2303–2317.

Shields, A., 1936. Anwendung der anhlichkeitsmechanik und turbulenzforschung auf die geschiebebewegung. In: Mitt. Preuss Versuchsanstalt fur Wassebaur und Schiffbau, vol 26.

Sleath, J.F.A., 1999. Conditions for plug formation in oscillatory flow. Cont. Shelf Res. 19, 1643–1664.

Sumer, B.M., Laursen, T.S., Fredsøe, J., 1993. Wave boundary layer in a convergent tunnel. Coast. Eng. 20, 317–342.

Sumer, B.M., Kozakiewicz, A., Fredsøe, J., Deigaard, R., 1996. Velocity and concentration profiles in sheet-flow layer of movable bed. J. Hydr. Eng. 122 (10), 549–558.

Suzuki, T., Shin, S., Cox, D.T., Mori, N., 2010. Spatiotemporal characteristics of near-bed pressure gradients on a barred beach. J. Waterw. Port, Coast. Ocean Eng. 136 (December), 327–336. https://doi.org/10.1061/(ASCE)WW.1943-5460.0000055.

Thornton, E.B., Humiston, R.T., Birkemeier, W., 1996. Bar/trough generation on a natural beach. J. Geophys. Res. 101 (C5), 12097–12110.

Tissier, M., Bonneton, P., Almar, R., Castelle, B., Bonneton, N., Nahon, A., 2011. Field measurements and non-linear prediction of wave celerity in the surf zone. Eur. J. Mech. B Fluid 30 (6), 635–641 2011.

Van der A, D.A., Ribberink, J.S., Van der Werf, J.J., O'Donoghue, T., Buijsrogge, R.H., Kranenburg, W.M., 2013. Practical sand transport formula for non-breaking waves and currents. Coast. Eng. 76, 26–42. https://doi.org/10.1016/j.coastaleng.2013.01.007.

Voulgaris, G., Collins, M.B., 2000. Sediment resuspension on beaches: response to breaking waves. Mar. Geol. 67, 167–197.

Wang, Y.–H., Yu, G.–H., 2007. Velocity and concentration profiles of particle movement in sheet flows. Adv. Water Resour. 30 (5), 1355–1359. https://doi.org/10.1016/j.advwatres.2006.11.012.

Watanabe, A., Sato, S., 2004. A sheet-flow transport rate formula rate formula for asymmetric forward-leaning waves and currents. In: Proc. 29th Conf. Coast. Eng. World Scientific, pp. 1703–1714. https://doi.org/10.1142/9789812701916_0136.

Willmott, C.J., 1981. On the validation of models. Phys. Geogr. 2, 184–194. https://doi.org/10.1080/02723646.1981.10642213.

Willmott, C.J., Wicks, D.E., 1980. An empirical method for the spatial interpolation of monthly precipitation within California. Phys. Geogr. 1, 59–73. https://doi.org/10.1080/02723646.1980.10642189.

Yoon, H.D., Cox, D.T., 2010. Large-scale laboratory observations of wave breaking turbulence over an evolving beach. J. Geophys. Res. 115, C10007. https://doi.org/10.1029/2009JC005748.